JOURNAL OF GEOPHYSICAL RESEARCH, VOL. 113, D15201, doi:10.1029/2007JD009354, 2008



# Aerosol-cloud relationships in continental shallow cumulus

Miao-Ling Lu,[1] Graham Feingold,[2] Haflidi H. Jonsson,[3] Patrick Y. Chuang,[4] Harmony Gates,[5] Richard C. Flagan,[1,6] and John H. Seinfeld[1,6]

Received 4 September 2007; revised 29 February 2008; accepted 12 May 2008; published 5 August 2008.

[1] Aerosol-cloud relationships are derived from 14 warm continental cumuli cases sampled during the 2006 Gulf of Mexico Atmospheric Composition and Climate Study (GoMACCS) by the Center for Interdisciplinary Remotely-Piloted Aircraft Studies (CIRPAS) Twin Otter aircraft. Cloud droplet number concentration is clearly proportional to the subcloud accumulation mode aerosol number concentration. An inverse correlation between cloud top effective radius and subcloud aerosol number concentration is observed when cloud depth variations are accounted for. There are no discernable aerosol effects on cloud droplet spectral dispersion; the averaged spectral relative dispersion is 0.30 ± 0.04. Aerosol-cloud relationships are also identified from comparison of two isolated cloud cases that occurred under different degrees of anthropogenic influence. Cloud liquid water content, cloud droplet number concentration, and cloud top effective radius exhibit subadiabaticity resulting from entrainment mixing processes. The degree of LWC subadiabaticity is found to increase with cloud depth. Impacts of subadiabaticity on cloud optical properties are assessed. It is estimated that owing to entrainment mixing, cloud LWP, effective radius, and cloud albedo are decreased by 50–85%, 5–35%, and 2–26%, respectively, relative to adiabatic values of a plane-parallel cloud. The impact of subadiabaticity on cloud albedo is largest for shallow clouds. Results suggest that the effect of entrainment mixing must be accounted for when evaluating the aerosol indirect effect.

**Citation:** Lu, M.-L., G. Feingold, H. H. Jonsson, P. Y. Chuang, H. Gates, R. C. Flagan, and J. H. Seinfeld (2008), Aerosol-cloud relationships in continental shallow cumulus, *J. Geophys. Res.*, *113*, D15201, doi:10.1029/2007JD009354.

## 1. Introduction

[2] Extensive theoretical and observational studies of aerosol-cloud interactions and indirect effects on maritime stratocumulus exist (see, for example, summary by *Lu et al.* [2007, Table 3]). Considerably fewer studies have systematically examined aerosol effects on warm continental cumuli. Relative to marine stratocumulus, continental shallow cumulus exhibit more transient evolution, with cloud lifetimes lasting about 30 min up to 1 h or so. Surface-driven convection causes these clouds to be susceptible to mixing processes, which play an important role in cloud structure and dynamics.

[3] Observational evidence of aerosol (or indirect, for radiative response) effects on continental warm clouds does exist. On the basis of 60-year ground station rainfall data in Australia, *Warner* [1968] found a reduction in precipitation during the sugarcane harvesting season, an effect attributed to reduced droplet coalescence as a result of smoke-induced smaller cloud droplets. However, more rigorous analysis [*Warner*, 1971] failed to produce a clear signal for aerosol effects on surface precipitation. *Rosenfeld and Lensky* [1998] noted that on the basis of satellite data, convective cumulus/trade wind cumulus clouds that undergo transitions from maritime to continental conditions (from eastern Mediterranean/western Pacific to inland) exhibit smaller cloud top droplet sizes and less effective warm rain formation over land than over ocean. Statistically strong evidence of orographic precipitation suppression by anthropogenic pollution downwind of the pollution sources has been shown by *Jirak and Cotton* [2006]. Data from the Aerosol Robotic Network (AERONET) global Sun photometer ground sites show that cloud cover in the presence of pollution increases with increasing aerosol column concentration [*Kaufman and Koren*, 2006]. Ground-based remote sensing observations of single layer clouds in Oklahoma showed the influence of aerosol loading in reducing the cloud drop effective radius [*Feingold et al.*, 2003; *Kim et al.*, 2003] or changing the shortwave radiative fluxes [*Penner et al.*, 2004] at constant liquid water path.

[4] The goal of this work is to explore the extent to which aerosol-cloud relationships are evident in the warm shallow

[1]Department of Environmental Science and Engineering, California Institute of Technology, Pasadena, California, USA.
[2]Chemical Sciences Division, Earth System Research Laboratory, NOAA, Boulder, Colorado, USA.
[3]Department of Meteorology, Naval Postgraduate School, Monterey, California, USA.
[4]Department of Earth and Planetary Sciences, University of California, Santa Cruz, California, USA.
[5]Department of Chemical Engineering, California Institute of Technology, Pasadena, California, USA.
[6]Also at Department of Chemical Engineering, California Institute of Technology, Pasadena, California, USA.


0148-0227/08/2007JD009354$09.00

**Table 1.** Instrument Payload on Board the CIRPAS Twin Otter[a] in GoMACCS

| Instrument | Data[b] |
|---|---|
| Condensation particle counter (CPC) | aerosol number concentration (CPC 3025, >3 nm; CPC 3010, >10 nm, dry) |
| Counterflow virtual impactor (CVI) | virtual impactor for isolating cloud droplets (cut size of 10 $\mu$m ± 20%) |
| Dual automated classified aerosol detector (DACAD) | submicrometer aerosol size distribution (10.3–828 nm, 85 bins) at two RHs (dry and wet) |
| Passive cavity aerosol spectrometer probe (PCASP), forward scattering spectrometer probe (FSSP), cloud/aerosol/precipitation spectrometer (CAPS consists of cloud and aerosol spectrometer (CAS) and cloud imaging probe (CIP)), phase Doppler interferometer (PDI [*Chuang et al.*, 2008]) | aerosol/cloud/precipitation droplet size distribution: PCASP (0.1–2.6 $\mu$m, dry), FSSP[c] (2.55–42.7 $\mu$m, 19 bins), CAS[c,d] (0.54–62 $\mu$m, 20 bins), CIP[c] (40.45 $\mu$m–1.56 mm, 61 bins), PDI[c,e] (2.07–200 $\mu$m, 127 bins) |
| Time-of-flight Aerodyne aerosol mass spectrometer (TOF-AMS) | nonrefractory aerosol chemistry |
| Particle-into-liquid sampler/ion chromatography (PILS-IC [*Sorooshian et al.*, 2006]) | submicrometer water-soluble aerosol chemistry (inorganic and organic acid ions) |
| Solar spectral flux radiometer (SSFR [*Pilewskie et al.*, 2003]) | upwelling and downwelling radiative fluxes above and below cloud |
| Particle soot absorption photometer (PSAP), photoacoustic spectrometer, $CO_2$ | soot absorption (multiwavelength/incandescence) |
| Navigational/meteorology probes and Gerber liquid water content probe (PVM-100A [*Gerber et al.*, 1994]), hotwire LWC probe | navigational data, temperature, dew point, RH, pressure, liquid water content, wind direction/speed, updraft velocity, etc. |
| Cloud condensation nuclei counter (CCN [*Roberts and Nenes*, 2005]) | CCN at different supersaturations |
| Multiangle light scattering spectrometer (MLS) | shape and angular dependence of light scattering of individual particles |

[a]Aircraft flight speed of ~50 m $s^{-1}$.
[b]All sizes are in diameter.
[c]First bin has been omitted.
[d]CAS data were available before 2 September.
[e]PDI data were undergoing calibration at the time of writing.

continental cumuli sampled during the 2006 Gulf of Mexico Atmospheric Composition and Climate Study (GoMACCS). A brief summary of the GoMACCS experiment is given in section 2. Section 3 presents observational data on cloud properties from GoMACCS. Section 4 explores the effect of entrainment mixing processes on observed cloud properties, including the sensitivity of cloud albedo to entrainment. This work provides clear and systematic observational data for aerosol-cloud relationships in continental cumuli.

## 2. GoMACCS Experiment

[5] The GoMACCS (http://esrl.noaa.gov/csd/2006/) was conducted jointly with the 2006 TexAQS (Texas Air Quality Study) during August and September 2006 as a combined climate change and air quality intensive field campaign. During the GoMACCS campaign, the Center for Interdisciplinary Remotely-Piloted Aircraft Studies (CIRPAS) Twin Otter (see instrument payload in Table 1 and http://www.cirpas.org) performed 22 research flights to explore aerosol-cloud relationships over the Houston region and the northwestern Gulf of Mexico. Flight paths of all research flights are shown in Figure 1.

[6] Among the 22 research flights conducted by the Twin Otter, fourteen intensive cloud measurements (cloud top <4 km) were carried out, including three (RF16_2, RF18, and RF19_2) in which isolated cumulus clouds of sufficient size and lifetime existed to allow detailed

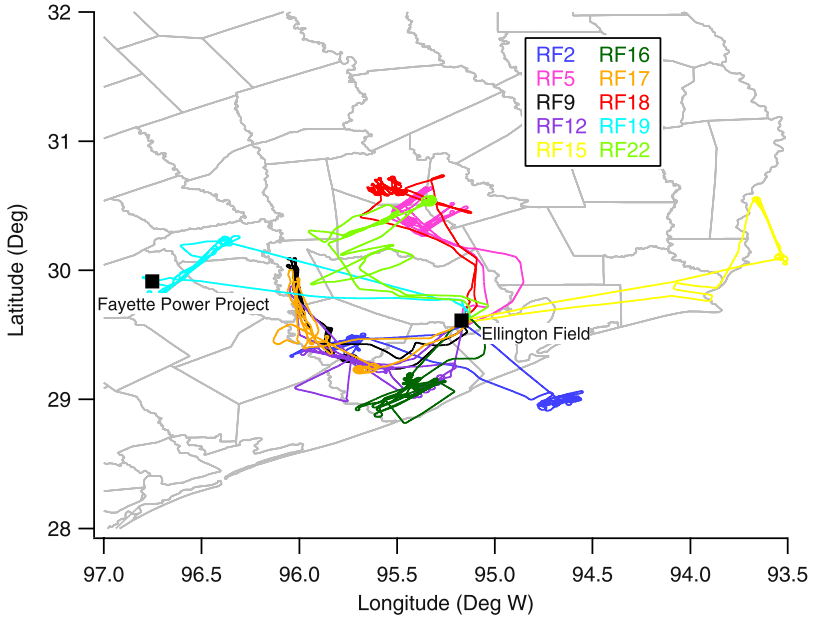


**Figure 1.** Flight paths of all mission flights in GoMACCS.

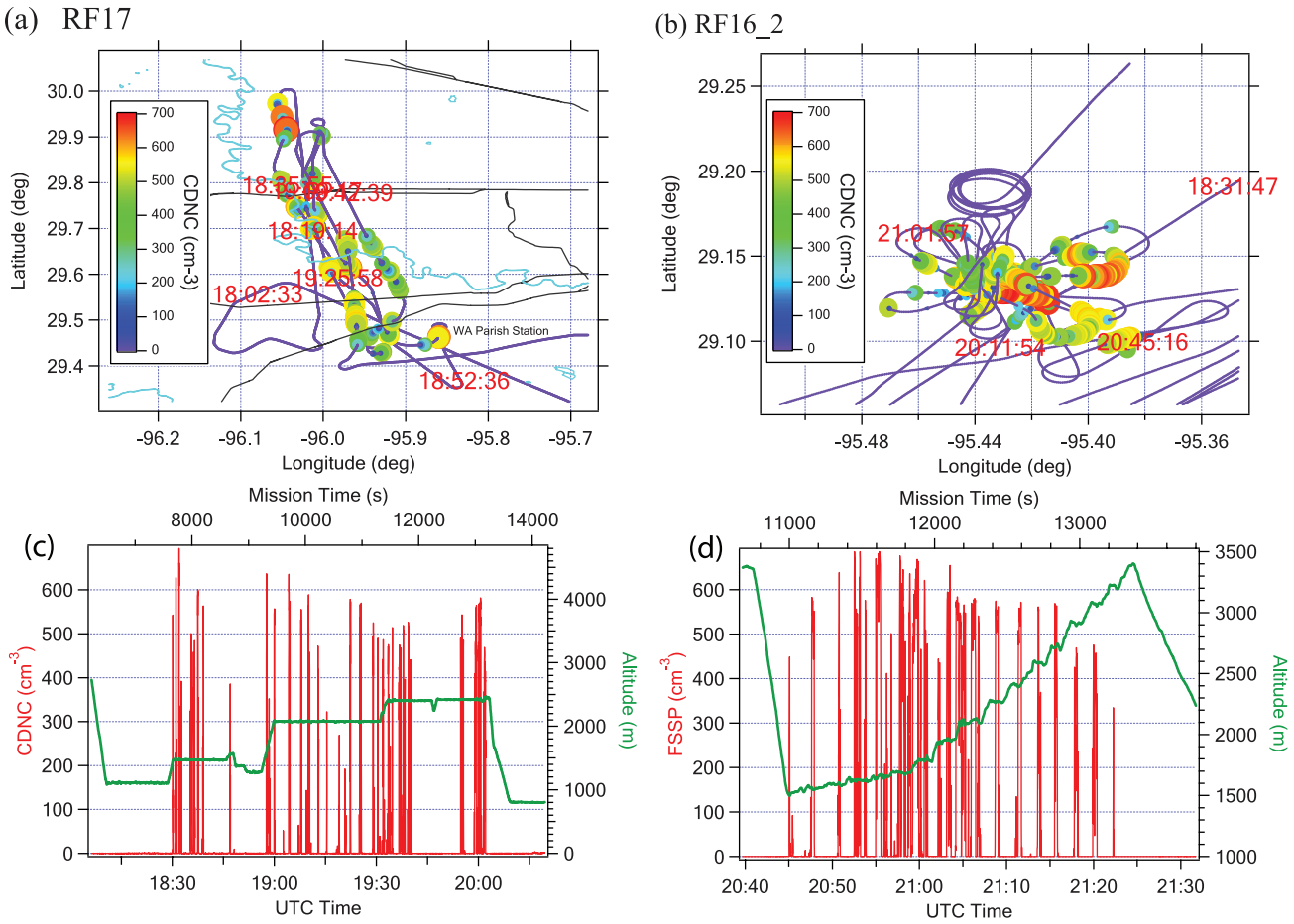


**Figure 2.** (a and b) Flight path colored according to the value of CDNC and (c and d) time series of altitude and CDNC for a cloud fields sampled during RF17 (Figures 2a and 2c) and for a single cloud sampled during RF16_2 (Figures 2b and 2d).

sampling; the other 11 cases involved scattered cumuli that were sampled in such a manner as to provide statistical properties over the cloud field. The flight paths and time series of altitude and CDNC for both cloud field and isolated clouds are shown in Figure 2. Comparisons of the statistical properties of simulated and observed cumuli are presented in the companion work of *Jiang et al.* [2008]. Flights that focused on atmospheric composition studies are described by *Sorooshian et al.* [2007]. The clouds sampled were all continental warm cumulus clouds subject to various levels of anthropogenic influence, as characterized by the subcloud aerosol concentration. Each cloud case was characterized by cloud profiling; that is, at least one subcloud or cloud base horizontal flight leg, one in-cloud leg, and one cloud top leg were carried out. Additional horizontal passes through the cloud were carried out, particularly for the isolated cloud cases. Table 2 summarizes the properties of the sampled clouds. The cloud top and base were determined visually by the pilot during the sampling period and from the highest and lowest horizontal flight passes at which nonzero cloud LWC was recorded. For the cases involving scattered cumuli, the cloud top, by this definition, is the highest cloud top among all cumuli during the sampling period. The cloud base determined in this manner is compared with the calculated lifting condensation level (LCL) of the below-cloud unsaturated air parcel in Table 3. Cloud bases estimated on the basis of visual observation and in-flight data lie mostly within 10% of the calculated LCL.

[7] Cloud properties are calculated using the FSSP probe spectral data with upper cutoff size of ~21 $\mu$m (in radius). The first bin of spectral data from the cloud probes (Table 1) is neglected owing to measurement uncertainty associated with this bin. Droplet coincidence losses in the FSSP laser beam have been taken into account in the measured droplet number concentrations following *Baumgardner et al.* [1985]. The term "leg mean" designates the mean value calculated over each horizontal flight leg. The mean cloud droplet number concentration (CDNC) for a cloud as given in Table 2 was obtained by vertical averaging of the flight leg means, over the cloudy regions, with caution to avoid the exceptionally small values near cloud top or base. The maximum CDNC reported for each case is the averaged FSSP data of the cloud base leg.. The maximum CDNC value is that which is considered to be least influenced by any entrainment processes and thus is considered as a proxy for the adiabatic CDNC ($CDNC_{ad}$). Cloud LWC (and effective radius) typically increases monotonically with height in the cloud; the cloud top LWC (and effective radius) reported in Table 2 is the leg mean value at the cloud top leg or, if appropriate, the average over several legs

**Table 2.** Summary of Properties of Clouds Observed During GoMACCS (2006)[a]

| RF Number | Date, UTC | CDNC,[b] $cm^{-3}$ | Updraft Mean CDNC, $cm^{-3}$ | Maximum CDNC, $cm^{-3}$ | Cloud Top LWC, g $m^{-3}$ | Cloud Top $r_e$,[b] $\mu$m | $N_a$,[b] $cm^{-3}$ | $N_{acc}$,[b] $cm^{-3}$ | Cloud Base, m | Cloud Top, m | Mean Updraft Velocity,[b] m $s^{-1}$ | Cloud Top Relative Dispersion[b] | Cloud Top $k$[b] | $C_w$, g $m^{-3}$ $km^{-1}$ | Cloud Top $AR_L$ | $AR_N$ |
|---|---|---|---|---|---|---|---|---|---|---|---|---|---|---|---|---|
| 2 | 22 Aug, 1621–1803 | 300 (199)[c] | 397 (87) | 648 | 0.29 | 6.0 | 1420 (294) | 556 (48) | 630 | 1047 | 0.71 (0.58) | 0.3 | 0.78 | 2.38 | 0.29 | 0.46 |
| 5_1 | 26 Aug, 1520–1634 | 172 (121) | 282 (85) | 392 | 0.76 | 9.4 | 1884 (347) | 429 (70) | 974 | 2080 | 0.45 (0.45) | 0.33 | 0.77 | 2.36 | 0.29 | 0.44 |
| 5_2 | 26 Aug, 1638–1741 | 196 (121) | 320 (37) | 418 | 0.61 | 9.7 | 1408 (506) | 437 (49) | 1280 | 2403 | 0.65 (0.69) | 0.28 | 0.82 | 2.32 | 0.23 | 0.47 |
| 9_1 | 29 Aug, 1458–1647 | 269 (188) | 572 (84) | 729 | 0.36 | 7.3 | 5063 (3119) | 714 (172) | 778 | 1247 | 0.64 (0.57) | 0.32 | 0.79 | 2.34 | 0.33 | 0.37 |
| 9_2 | 29 Aug, 1647–1752 | 239 (158) | 390 (103) | 524 | 0.27 | 6.0 | 3443 (1134) | 526 (41) | 1200 | 1596 | 0.63 (0.93) | 0.31 | 0.76 | 2.29 | 0.30 | 0.46 |
| 12 | 2 Sep, 1703–2021 | 322 (221) | 506 (160) | 665 | 0.33 | 5.4 | 5026 (2216) | 1447 (202) | 1424 | 2420 | 0.69 (0.77) | 0.32 | 0.76 | 2.25 | 0.15 | 0.48 |
| 15 | 6 Sep, 1759–2026 | 299 (179) | 439 (101) | 728 | 1.07 | 9.7 | 2159 (428) | 1003 (137) | 1774 | 3996 | 0.57 (0.70) | 0.26 | 0.83 | 2.12 | 0.23 | 0.41 |
| 16_1 | 7 Sep, 1832–2042 | 366 (231) | 520 (181) | 745 | 0.62 | 6.5 | 9089 (5345) | 1506 (156) | 1615 | 2718 | 0.89 (1.00) | 0.28 | 0.80 | 2.05 | 0.27 | 0.49 |
| 16_2[d] | 7 Sep, 2045–2125 | 425 (239) | 481 (221) | 860 | 0.63 | 7.3 | 5191 (139) | 1639 (160) | 1530 | 3200 | 1.23 (0.95) | 0.31 | 0.77 | 2.18 | 0.17 | 0.49 |
| 17 | 8 Sep, 1809–2004 | 340 (228) | 473 (175) | 851 | 0.45 | 6.4 | 7496 (2633) | 1582 (215) | 1478 | 2410 | 0.75 (0.74) | 0.31 | 0.78 | 2.21 | 0.22 | 0.40 |
| 18[e] | 10 Sep, 1629–1744 | 267 (138) | 311 (115) | 620 | 1.24 | 11.0 | 2046 (1316) | 614 (57) | 794 | 3367 | 1.18 (1.11) | 0.27 | 0.84 | 2.30 | 0.21 | 0.43 |
| 19_1 | 11 Sep, 1553–1716 | 218 (145) | 403 (62) | 627 | 0.69 | 10.5 | 11500 (9051) | 595 (129) | 1288 | 3140 | 0.53 (0.54) | 0.4 | 0.66 | 2.29 | 0.16 | 0.35 |
| 19_2[d] | 11 Sep, 1716–1801 | 283 (190) | 447 (144) | 794 | 0.75 | 7.9 | 11048 (9098) | 595 (129) | 1227 | 2440 | 1.80 (1.01) | 0.29 | 0.79 | 2.28 | 0.27 | 0.36 |
| 22 | 15 Sep, 1626–1810 | 294 (193) | 550 (94) | 752 | 0.84 | 9.1 | 3355 (576) | 903 (165) | 976 | 2757 | 0.61 (0.62) | 0.25 | 0.84 | 2.33 | 0.20 | 0.39 |
| Average | | | | | | | | | | | | | 0.30 (0.04) | 0.78 (0.05) | 2.26 (0.10) | 0.43 (0.05) |

[a]The minimum threshold values for calculating the mean CDNC, LWC, $r_e$, relative dispersion, and $k$ are 10 $cm^{-3}$, 0.05 g $m^{-3}$, 0.05 $\mu$m, 0.05, and 0.05, respectively. Therefore, the cloud properties are calculated over the cloudy regions.
[b]Leg mean properties.
[c]The number in parentheses is one standard deviation.
[d]Single cloud.
[e]Two individual clouds; the rest are cloud fields.

**Table 3.** Cloud Base and the Calculated Lifting Condensation Level[a]

| RF Number | Cloud Base (m) | LCL (Iteration [*Seinfeld and Pandis*, 2006]) (m) | LCL (Approximate Formula [*Bolton*, 1980]) (m) |
|---|---|---|---|
| 2 | 630 | 687 | 671 |
| 5_1 | 974 | 957 | 953 |
| 5_2 | 1280 | 1314 | 1273 |
| 9_1 | 778 | 809 | 838 |
| 9_2 | 1200 | 1076 | 1208 |
| 12 | 1424 | 1602 | 1588 |
| 15 | 1774 | 1674 | 1615 |
| 16_1 | 1615 | 1562 | 1615 |
| 16_2 | 1530 | 1465 | 1442 |
| 17 | 1478 | 1404 | 1432 |
| 18 | 794 | 923 | 931 |
| 19_1 | 1288 | 1381 | 1268 |
| 19_2 | 1227 | 1243 | 1268 |
| 22 | 976 | 947 | 947 |

[a]LCL, lifting condensation level.

near cloud top. Cloud spectral relative dispersion is related to effective radius, and therefore is also calculated from the leg mean values near cloud top [see also *Lu and Seinfeld*, 2006]. Subcloud total/accumulation-mode aerosol number concentration represents the mean value of the CPC/PCASP counts measured on the subcloud leg. The total aerosol number concentration (as measured by the CPC) is denoted as $N_a$. The predominance of particles measured by the PCASP are in the accumulation mode; we therefore denote the PCASP measured aerosol number concentration as $N_{acc}$. Updraft velocity ($w > 0$) is reported as the leg mean value measured at the cloud base; $\sigma_w$ is the standard deviation of updraft velocity. Raindrop number concentration and rain liquid water content are measured by the CIP with lower cutoff size of 20 $\mu$m (in radius). Given the fact that the largest value of maximum rain number concentration is about $\sim$0.2 cm$^{-3}$ (RF18) among all cloud cases, with other clouds exhibiting values far less than this, the clouds sampled in GoMACCS are essentially nonprecipitating.

## 3. Aerosol-Cloud Relationships in GoMACCS

[8] Aerosol-cloud relationships for all clouds sampled during the GoMACCS experiment are summarized in Figure 3. Subcloud aerosol concentrations exhibit a wide range of values, with $N_a$ ranging from 1400 to 11,500 cm$^{-3}$ and $N_{acc}$ from 400 to 1650 cm$^{-3}$. Figure 3a shows leg mean cloud droplet number concentration (CDNC) versus subcloud total aerosol number concentration ($N_a$). Excluding two cloud cases (RF19_1 and RF19_2, discussed below), the data show a general trend of increasing CDNC with increasing subcloud total aerosol concentration, and can be fit with a power law relationship. Figure 3b depicts the analogous relationship between the subcloud accumulation mode aerosol number concentration ($N_{acc}$) and CDNC ($CDNC = 15.3\ N_{acc}^{0.43}$, $R^2 = 0.77$ or $CDNC_{ad} = 55.0\ N_{acc}^{0.37}$, $R^2 = 0.57$, when $CDNC_{ad}$ is used (not shown)). A better regression is obtained from the data as represented in Figure 3b than in Figure 3a, which indicates that some portion of $N_a$ is composed of small particles that do not activate.

[9] The two cases, RF19_1 and RF19_2, represent cumuli observed in the vicinity of a coal-burning power plant (Fayette Power Project), where the measured subcloud total aerosol number concentration was the highest among all cases. These two clouds exhibit much smaller CDNC than predicted by the overall regression in Figure 3a; when expressed in terms of the accumulation mode aerosol (Figure 3b), data for these two cases lie on the line for the other cases sampled. This suggests that the power plant plume contained numerous nonactivating small particles; the DACAD data for these two cases show that 88% of $N_a$ are below 50 nm. In summary, a tighter aerosol-cloud relationship is obtained by using $N_{acc}$ rather than $N_a$ because most of the CCN reside in the accumulation mode.

[10] The PCASP has a lower cutoff size of 100 nm (corresponding to 0.15% critical supersaturation from Köhler theory for ammonium sulfate at ambient temperature of 20°C); undetected particles smaller than this size might become activated and thereby affect the regression in Figure 3b. Sensitivity of the aerosol number concentration with different lower cutoff sizes than the PCASP detection limit is explored by adding the particles measured by the DACAD between size $z$ to 100 nm ($N_{a,\ z-100\ \mathrm{nm}}$, where $z$ = 60, 70, and 83 nm in dry diameter, corresponding to 0.33–0.20% critical supersaturation) to $N_{acc}$. Considering CDNC with $N_{acc} + N_{a,\ z-100\ \mathrm{nm}}$ in Table 4 shows that the regression is not improved (judged from $R^2$) after including these smaller particles, which suggests that particles larger than 100 nm are the principal ones activated. The updraft velocity is another important factor that determines the maximum supersaturation achieved in the cloud, which also affects the number of activated droplets. Similar to previous findings in stratocumulus [*Lu et al.*, 2007], better regressions result when both $N_{acc}$ and updraft velocity ($w$) are taken into account,

$$CDNC = 21.09\ N_{acc}^{0.39}\ w^{0.21},\ \left(R^2 = 0.87\right)$$
$$CDNC_{ad} = 77.61\ N_{acc}^{0.33}\ w^{0.23},\ \left(R^2 = 0.68\right) \quad (1)$$

*Feingold* [2003] evaluated the sensitivity of $r_e$ to several aerosol and cloud properties from an adiabatic cloud parcel model. He found that for conditions gradually changing from clean to polluted, the relative importance of $w$ in determining $r_e$ increases significantly while that of $N_a$ decreases. GoMACCS clouds are considered as polluted clouds by his definition and the results of sensitivity of $r_e$ is applicable to sensitivity of CDNC through the relationship of $r_e \propto (\mathrm{LWC/CDNC})^{1/3}$. We assess the relative importance of $N_{acc}$ and updraft velocity in determining CDNC of GoMACCS clouds by the partial derivatives, $\frac{\partial \ln CDNC}{\partial \ln N_{acc}} = 0.39$ and $\frac{\partial \ln CDNC}{\partial \ln w} = 0.21$. The partial derivative results indicate that variations in $w$ account for about half the contribution of $N_{acc}$ to CDNC.

### 3.1. Droplet Activation Ratio

[11] The droplet activation ratio, defined as the ratio of updraft mean CDNC to $N_{acc}$, is high ($\sim$80%) for low $N_{acc}$ values and low ($\sim$40%) at high $N_{acc}$ (Figure 3d). Clouds having these two different activation ratio values exhibited similar updraft velocities in the range of 0.5–0.9 m s$^{-1}$. This result is consistent with observations of polluted marine cumuli reported by *Raga and Jonas* [1993] (who

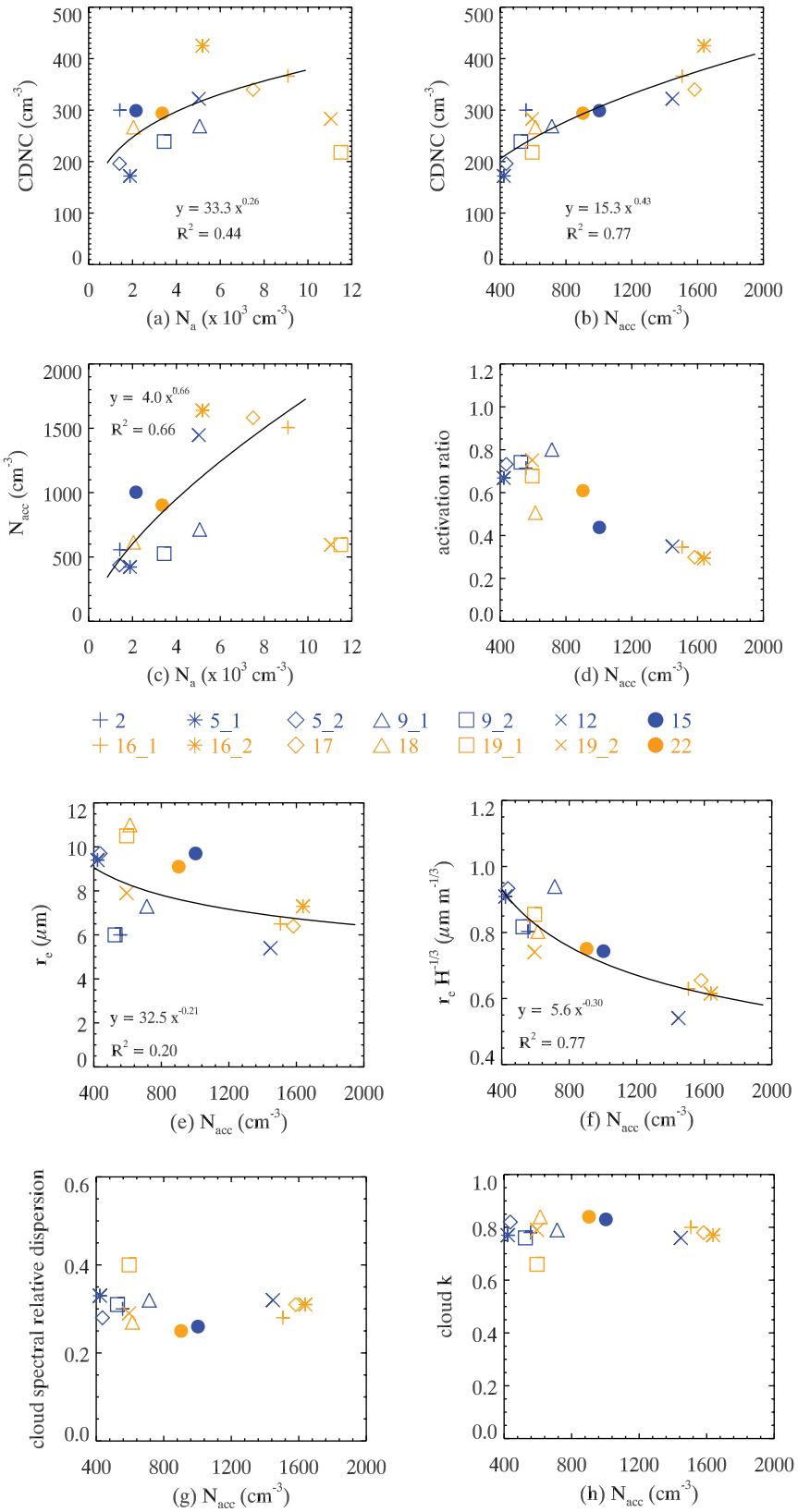


**Figure 3.** Aerosol-cloud relationships from all sampled clouds. (a) Subcloud total aerosol number concentration ($N_a$) versus leg mean cloud droplet number concentration (CDNC), (b) subcloud accumulation mode aerosol number concentration ($N_{acc}$) versus CDNC, (c) $N_a$ versus $N_{acc}$, (d) $N_{acc}$ versus droplet activation ratio, (e) $N_{acc}$ versus cloud top effective radius and (f) effective radius scaled by cloud depth, (g) $N_{acc}$ versus cloud spectral relative dispersion, and (h) $N_{acc}$ versus cloud top $k$. Solid lines are the regression results for all clouds except where Figure 3a excludes RF19_1 and RF19_2.

**Table 4.** Dependence of CDNC on Aerosol Number Concentration at Different Minimum Cutoff Sizes

| Aerosol Number Concentration | Regression Results | $R^2$ |
|---|---|---|
| $N_{acc}$ | $y = 15.3\ x^{0.43}$ | 0.77 |
| $N_{acc} + N_{a,83-100\ nm}$ | $y = 18.7\ x^{0.39}$ | 0.74 |
| $N_{acc} + N_{a,70-100\ nm}$ | $y = 19.9\ x^{0.37}$ | 0.74 |
| $N_{acc} + N_{a,60-100\ nm}$ | $y = 20.3\ x^{0.36}$ | 0.73 |

used the ratio of maximum CDNC to $N_{acc}$) and of continental cumuli by *Leaitch et al.* [1986]. The decrease of activation fraction with increasing aerosol number concentration arises because of the lowered maximum supersaturation owing to competition for available water vapor.

### 3.2. Cloud Droplet Effective Radius

[12] The cloud droplet effective radius ($r_e$) is defined as the ratio of the third moment to the second moment of the cloud droplet size distribution. Figure 3e shows the relationship between cloud top effective radius and subcloud $N_{acc}$. Because the cloud top $r_e$ depends also on cloud depth ($H$), $r_e \propto (H/\mathrm{CDNC})^{1/3}$ (see also later equation (6) or *Brenguier et al.* [2000] and *Boers et al.* [2006]), to obtain a clearer relationship between $r_e$ and $N_{acc}$, the variability in cloud depth can be incorporated by plotting $r_e/H^{1/3}$ against $N_{acc}$. Such a representation (Figure 3f) suggests that droplets in clouds subject to higher $N_{acc}$ have smaller effective radius; the power of $-0.30$ is close to the expected $-1/3$.

### 3.3. Cloud Droplet Spectral Dispersion

[13] Cloud droplet spectral relative dispersion is defined as the ratio of cloud droplet spectral width (the standard deviation of the drop size distribution, $\sigma$) to the cloud droplet mean radius ($d = \sigma/r_m$). Aerosol effects on cloud droplet spectral relative dispersion have been reported in several field measurements of cumuli/stratocumulus clouds [*Martin et al.*, 1994; *McFarquhar and Heymsfield*, 2001; *Liu and Daum*, 2002; *Lu et al.*, 2007]. No discernable relationship between aerosol number concentration and relative dispersion was observed for the continental cumuli in the current study (Figure 3g). The relative dispersion for all clouds sampled ranges from 0.28 to 0.4, with the average value of 0.30 ± 0.04 (one standard deviation). Large eddy simulations (LES) of marine stratocumulus by *Lu and Seinfeld* [2006] suggest that aerosol effects on relative dispersion occur when total aerosol number concentration is less than 1000 $\mathrm{cm}^{-3}$; in the current study generally $N_a >$ 1000 $\mathrm{cm}^{-3}$. The current observations are also consistent with those of *Miles et al.* [2000] for continental stratiform clouds, which show no evident relationship between relative dispersion and CDNC [see *Lu and Seinfeld*, 2006, Figure 16]. Measured GoMACCS aerosol and cloud droplet number concentrations are in the same range as those studied by *Miles et al.* [2000] and *Lu and Seinfeld* [2006]. The lack of a clear relationship between dispersion and $N_a$ might be due to the effect of aerosol chemical composition, or the variability of $w$. The inadequacy of the FSSP instrument to resolve the broadening of the distribution at the smaller drop end, where FSSP is well known not to be as reliable as at larger sizes, is also one of the possible factors. Dispersion effects are likely most evident for relatively pristine clouds as compared with those influenced by polluted air masses; pristine conditions were not encountered in GoMACSS.

[14] The coefficient $k$ is a parameter used to relate $r_e$ with $r_v$ (volume mean radius) in general circulation models (GCMs),

$$k = r_v^3/r_e^3. \tag{2}$$

$k$ is inversely dependent on $d$ for warm stratocumulus clouds [*Martin et al.*, 1994; *Lu and Seinfeld*, 2006]. (A monodisperse cloud droplet spectrum has unitary $k$.) Similar to $r_e$ and $d$, mean values of cloud top $k$ are derived for each sampled cloud (Table 2). We observed a strong inverse correlation between $k$ and $d$ with $R^2 = 0.93$ for GoMACCS clouds. The scatterplot of $k$ versus $N_{acc}$, as expected from the plot of $N_{acc}$-$d$, shows no correlation between the two parameters. The values of $k$ range from 0.66 to 0.84 with most lying close to the mean value of 0.78 ± 0.05. Widely cited values of $k$ and $d$ for marine stratocumulus are given by *Martin et al.* [1994], in which $k = 0.67$ ($d = 0.43$) and $k = 0.80$ ($d = 0.33$) for clouds influenced by continental and maritime air masses, respectively. In the Marine Stratus/Stratocumulus Experiment (MASE) [*Lu et al.*, 2007] mean values for all sampled stratocumulus clouds were $k = 0.75 \pm 0.08$ and $d = 0.30 \pm 0.06$. Interestingly, the continental cumulus clouds in GoMACCS exhibit similar values of $k$ and $d$ with those of the eastern Pacific coastal marine stratocumulus.

### 3.4. Aerosol-Cloud Microphysics Relationships

[15] Figures 4a–4c show the aerosol-cloud relationships from GoMACCS as well as those derived from other field measurements of shallow boundary layer clouds (*Raga and Jonas* [1993], *Martin et al.* [1994], North Atlantic Regional Experiment (NARE) [*Gultepe et al.*, 1996], Indian Ocean Experiment (INDOEX) [*McFarquhar and Heymsfield*, 2001], and MASE [*Lu et al.*, 2007]). The continental clouds sampled in the present study were subject to higher levels of anthropogenic influence than the other studies cited in Figure 4a. The clouds sampled in GoMACCS appear to be less efficient in activating droplets compared to the stratocumuli. For example, the exponent of the relationship between CDNC and $N_a$ is smaller for the GoMACCS clouds (0.26 versus 0.56) than that inferred from marine stratocumulus clouds in the MASE experiment [*Lu et al.*, 2007]. CDNC values in the GoMACCS clouds with $N_a < 2500\ \mathrm{cm}^{-3}$ are bounded by the two lines with updraft velocity between 0.5 and 2.0 m $\mathrm{s}^{-1}$ derived from the trade wind cumuli of INDOEX. The GoMACCS updraft velocities also lie within the range of these lines. *Raga and Jonas* [1993] measured marine cumuli over a comparable $N_{acc}$ range as that here. Figure 4b shows that the GoMACCS clouds exhibit larger CDNC than those in the work by *Raga and Jonas* [1993], which were measured near (<150 m) cloud top and may have been substantially influenced by entrainment. Figure 4b also shows that the GoMACCS results are close to those of *Martin et al.* [1994] under continental air masses and of *Gultepe et al.* [1996]. GoMACCS clouds exhibit slightly larger effective radius than those reported by *Raga and Jonas* [1993], but the trend of the $r_e$-$N_{acc}$ relationship is similar (Figure 4c).

[16] In general, a less steep CDNC-$N_a$ relationship from GoMACCS continental polluted cumuli exists than for the shallow cleaner clouds sampled in other studies. One of the

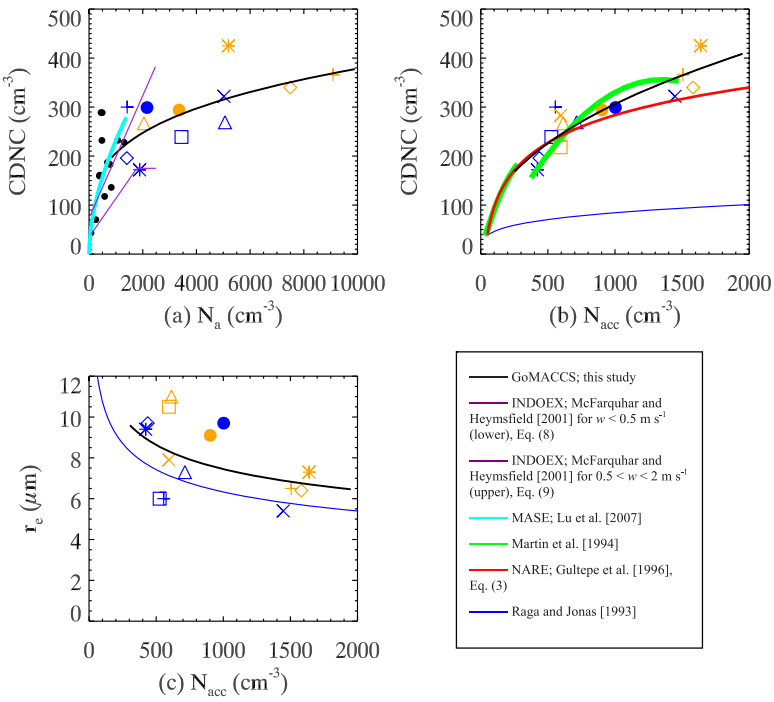


**Figure 4.** Comparison of (a) subcloud total aerosol number concentration and (b) subcloud accumulation mode aerosol number concentration versus cloud droplet number concentration and (c) cloud top effective radius versus $N_{acc}$ from GoMACCS with other field measurements (blue and orange symbols, see Figure 3 for definition). Two research flights with $N_a$ > 10,000 cm$^{-3}$ are excluded. INDOEX measured trade wind cumuli over the Indian Ocean, MASE measured marine stratocumulus off California coast, *Martin et al.* [1994] measured marine and continental stratocumulus; NARE measured marine stratus over east coast of Canada, and Raga and Jonas measured marine cumuli around the U.K. Black points are marine stratocumulus clouds from the MASE experiment [*Lu et al.*, 2007].

possible explanations is saturation at large aerosol loadings, as seen in the previous activation fraction data (Figure 3d). The distinctly different activation lines of the relatively cleaner shallow boundary layer clouds versus the polluted continental clouds sampled in the Houston area could also be related to differences in aerosol chemical composition between the two locations. The existence of an external mixture of hydrophobic aerosol, for example, could explain a low activation fraction.

[17] Aerosol-cloud relationships can be explored by comparing two isolated cloud cases (RF16_2 and RF18) that occurred under differing levels of anthropogenic influence. These two clouds were sampled during their active growing stages (visually determined by the pilot) at various altitudes for a total of ~1.5 h. Case RF16_2 was subject to about 2.5 times higher subcloud aerosol number concentration than RF18, which resulted in a factor of about 1.5 times higher CDNC (Figure 5a). The more polluted cloud shows a smaller effective radius throughout the cloud depth (solid line, Figure 5c). The cloud top effective radii are ~7 $\mu$m and ~10 $\mu$m for RF16_2 and RF18, respectively. The two cloud cases exhibit different LWC profiles and cloud bases and tops (Figure 5b). To remove these variabilities, $r_e$ is scaled by LWC$^{1/3}$ and exhibited against the normalized depth (= $h/H$, where $h$ is altitude above cloud base). Figure 5d shows that the scaled cloud effective radius is still smaller for the polluted case, which supports the findings in Figure 5c (solid line). One may postulate that the larger entrainment effect (because of the smaller $AR_L$ value in Table 2; see discussions in section 4) on $r_e$ for RF16_2 would lead to this smaller $r_e$ rather than owing to any effect of aerosols. The profiles of adiabatic $r_e$ (dotted line, Figure 5c; calculated by equation (6) subsequently) show that under adiabatic conditions, RF16_2 still has a smaller $r_e$ than RF18, suggesting that an aerosol effect is the cause of this difference.

[18] Although most of the clouds show negligible precipitation as noted in section 2, RF18 still exhibits some degree of precipitation and warrants further discussion. Figure 5e displays the vertical profile of precipitation rate. RF16_2 exhibits a cloud top precipitation rate about 10–100 times smaller than that of RF18. The cloud top rain LWC is about 20 times smaller (not shown). The rate of precipitation formation is represented in numerical models by the autoconversion rate, which is the rate that cloud LWC transfers to rain LWC. This rate is a function of LWC and CDNC, which is expressed as proportional to cloud LWC by powers ranging from 1 to 3 among various parameterizations [*Liu and Daum*, 2004]. Figure 5f shows the product of precipitation rate and LWC$^{-1}$ (solid lines) or LWC$^{-3}$ (dashed lines) as a function of altitude, in order to account for the variability in LWC (and also cloud depth). After this scaling, the precipitation rate is basically smaller throughout the cloud for the polluted case. We also compare the drizzle drop size for two cases. Figure 5g shows that the cleaner case (RF18) has a larger drizzle drop radius than the polluted case (RF16_2). In summary, these two cloud cases

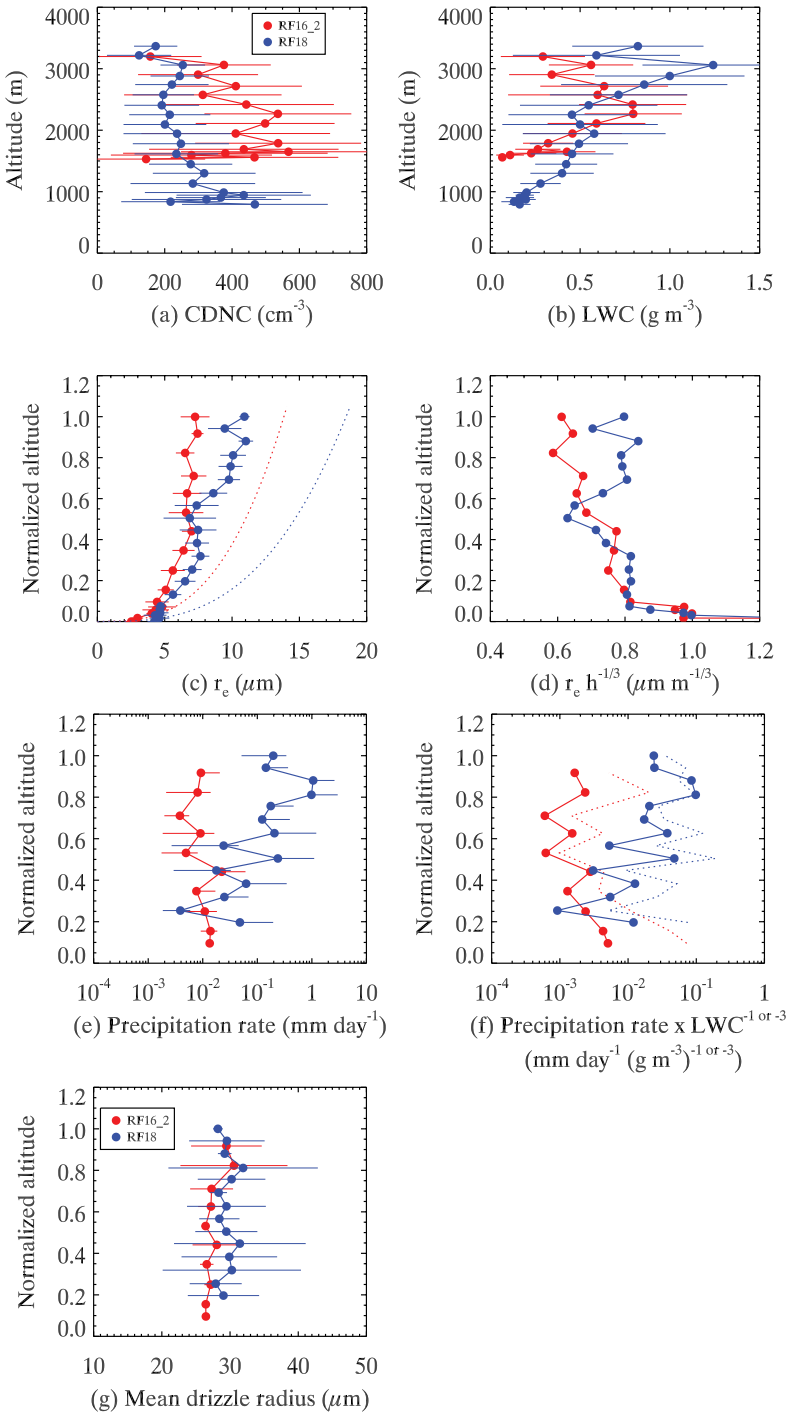


**Figure 5.** Vertical profiles of (a) CDNC, (b) LWC, (c) effective radius (measured leg mean, solid; calculated adiabatic value, dotted), (d) effective radius scaled by *LWC*, (e) precipitation rate, (f) precipitation rate scaled by LWC ($LWC^{-1}$, solid; $LWC^{-3}$, dotted), and (g) drizzle drop radius for two cloud cases representing different subcloud aerosol number concentration. Error bars represent the standard deviation around the mean. Normalized altitude represents height above cloud base normalized with respect to cloud depth.

confirm clearly that smaller cloud droplets, owing to a larger aerosol concentration, lead to less efficient collision coalescence and a smaller drizzle size and precipitation rate.

## 4. Effect of Entrainment Mixing on Cloud Properties

[19] Isolated cumuli or stratocumulus are frequently subject to entrainment of drier ambient air [*Warner*, 1955, 1970; *Boers et al.*, 2000; *Burnet and Brenguier*, 2007], which leads to dilution of LWC. The effects of entrainment were evident in the clouds sampled in GoMACCS. We address first the effect of entrainment on the vertical distribution of cloud LWC and effective radius for the deepest and shallowest cloud cases among all. Then, mixing events from the flight legs from these two cloud cases are identified. Last, the impacts of entrainment on cloud optical properties are assessed.

### 4.1. Entrainment Mixing Process

[20] When subsaturated ambient air is entrained and mixed with saturated cloudy air, the effect of the mixing process on cloud properties depends on the ratio of the turbulent mixing and droplet evaporation time constants [*Baker and Latham*, 1979; *Baker et al.*, 1980; *Burnet and Brenguier*, 2007]. On the basis of the value of this ratio, two types of mixing behavior have been identified. In so-called "homogeneous mixing" [*Warner*, 1973; *Mason and Jonas*, 1974], the rate of turbulent mixing exceeds that of droplet evaporation. Under this condition, a subsaturated cloudy mixture is formed upon dry air entrainment, and all droplets evaporate to smaller sizes at the same degree of undersaturation. In "inhomogeneous mixing" [*Baker and Latham*, 1979; *Baker et al.*, 1980], turbulent mixing occurs more slowly than droplet evaporation. In that case, droplet evaporation proceeds in the region immediately exposed to the entrained air; in the extreme case ("extremely inhomogeneous"), all droplets in this region evaporate, whereas droplet size in the unmixed region remains unchanged. Observational evidence for both mixing regimes exists, and both mixing regimes can, in principle, be present simultaneously, e.g., cumulus clouds in the work by *Burnet and Brenguier* [2007]. Entrainment into cumulus clouds can occur either laterally [*Raga et al.*, 1990] or at cloud top [*Paluch*, 1979; *Blyth and Latham*, 1985], with the latter interaction being more frequently observed. Regardless of the exact type of mixing, mixing processes eventually result in dilution of LWC and CDNC at the cloud scale.

[21] A useful diagnostic quantity to assess the extent to which entrainment is occurring is the LWC adiabatic ratio, $AR_L$, defined as

$$AR_L = LWC/LWC_{ad},\ AR_L \le 1, \tag{3}$$

the ratio of the actual LWC to that calculated assuming an adiabatic cloud profile. A smaller value of $AR_L$ implies larger liquid water dilution or greater departure from the adiabatic assumption. The adiabatic LWC can be expressed as a function of altitude $h$ above cloud base,

$$LWC_{ad} = C_w h. \tag{4}$$

The moist adiabatic condensation coefficient (or adiabatic LWC lapse rate), $C_w$ [g m$^{-3}$ km$^{-1}$], is a function of temperature and pressure [*Brenguier*, 1991],

$$C_w = 10^6 \rho_a^2 g\left(1 - \frac{c_p T}{\varepsilon L_v}\right)\left(\frac{c_p T}{\varepsilon L_v} + \frac{L_v w_{vs}\rho_a}{P - e_s}\right)^{-1}(\varepsilon e_s)(P - e_s)^{-2}, \tag{5}$$

where $\rho_a$ is air density (1 kg m$^{-3}$), $c_p$ is heat capacity of air at constant pressure (1005 J kg$^{-1}$ K$^{-1}$), $T$ is temperature (K), $\varepsilon = 0.622$ (the ratio of molecular weight of water to that of air), $L_v$ is latent heat of vaporization ($2.5 \times 10^6$ J kg$^{-1}$), $w_{vs}$ is saturation vapor mixing ratio (kg kg$^{-1}$), $P$ is pressure (Pa), $e_s$ is saturation vapor pressure (Pa), and $g$ is acceleration of gravity (9.8 m s$^{-2}$).

[22] To evaluate the extent to which $C_w$ varies from cloud base to cloud top, let us consider RF18 which exhibits the deepest cloud among all sampled clouds. The adiabatic LWC lapse rate below cloud top at $z$ = 3024 m with temperature of 8.9°C is 2.1 g m$^{-3}$ km$^{-1}$, close to its cloud base value (2.3 g m$^{-3}$ km$^{-1}$). Therefore, $C_w$ can be approximated as a constant value evaluated at cloud base. Most of the GoMACCS sampled clouds exhibited values of $C_w \cong 2.3$ g m$^{-3}$ km$^{-1}$ (Table 2). To help in interpreting the value of $AR_L$, following *Pawlowska et al.* [2006], $AR_L \ge 0.8$ is considered to be "quasi-adiabatic," $0.8 > AR_L \ge 0.5$ is "moderately diluted," $0.5 > AR_L \ge 0.1$ is termed "strongly diluted."

### 4.2. Case Studies

#### 4.2.1. RF18 (Deep Cloud, Strongly Diluted Case)

[23] RF18 was the deepest cloud case (cloud depth ~2600 m) among all those sampled. The vertical profile of LWC adiabatic ratio ($AR_L$) for RF18 is shown in Figure 6a. The leg mean $AR_L$ (solid gray line) is the average value of $AR_L$ for each horizontal flight segment through the cloud. These data show that the adiabatic region exists only near cloud base. Most of the cloud is strongly diluted and characterized by a value of $AR_L$ around 0.2–0.3, with the lowest $AR_L$ value occurring, as expected, at cloud top.

[24] One cannot rule out the possibility that a 1 Hz measurement frequency cloud probe is unable to capture transient peaks in LWC [*Gerber*, 2006]. Therefore, we examine the time series of high-frequency PVM-100A probe data (10 Hz) with the standard 1 Hz PVM-100A and FSSP data. The different measurements are consistent. Figure 7 shows that although the standard 1 Hz data are not capable of resolving some of the transient peaks in 10 Hz measurements, the general trend of data at two frequencies over one horizontal pass below cloud top are mutually consistent; furthermore, the leg mean of the three measurements are within 9% of each other. Given that our analysis focuses on horizontal averages, and also that 1 Hz cloud probes are the most widely used for cloud measurement, we report our findings based on this sampling frequency.

[25] In the absence of entrainment and precipitation, the cloud LWC would approach $LWC_{ad}$. Precipitation is one of the mechanisms that reduces the cloud LWC, but with a maximum rain LWC of 0.02 g m$^{-3}$, we can rule out precipitation as the explanation for the small $AR_L$ observed. One concludes that entrainment mixing is the main mechanism causing the LWC to deviate from its

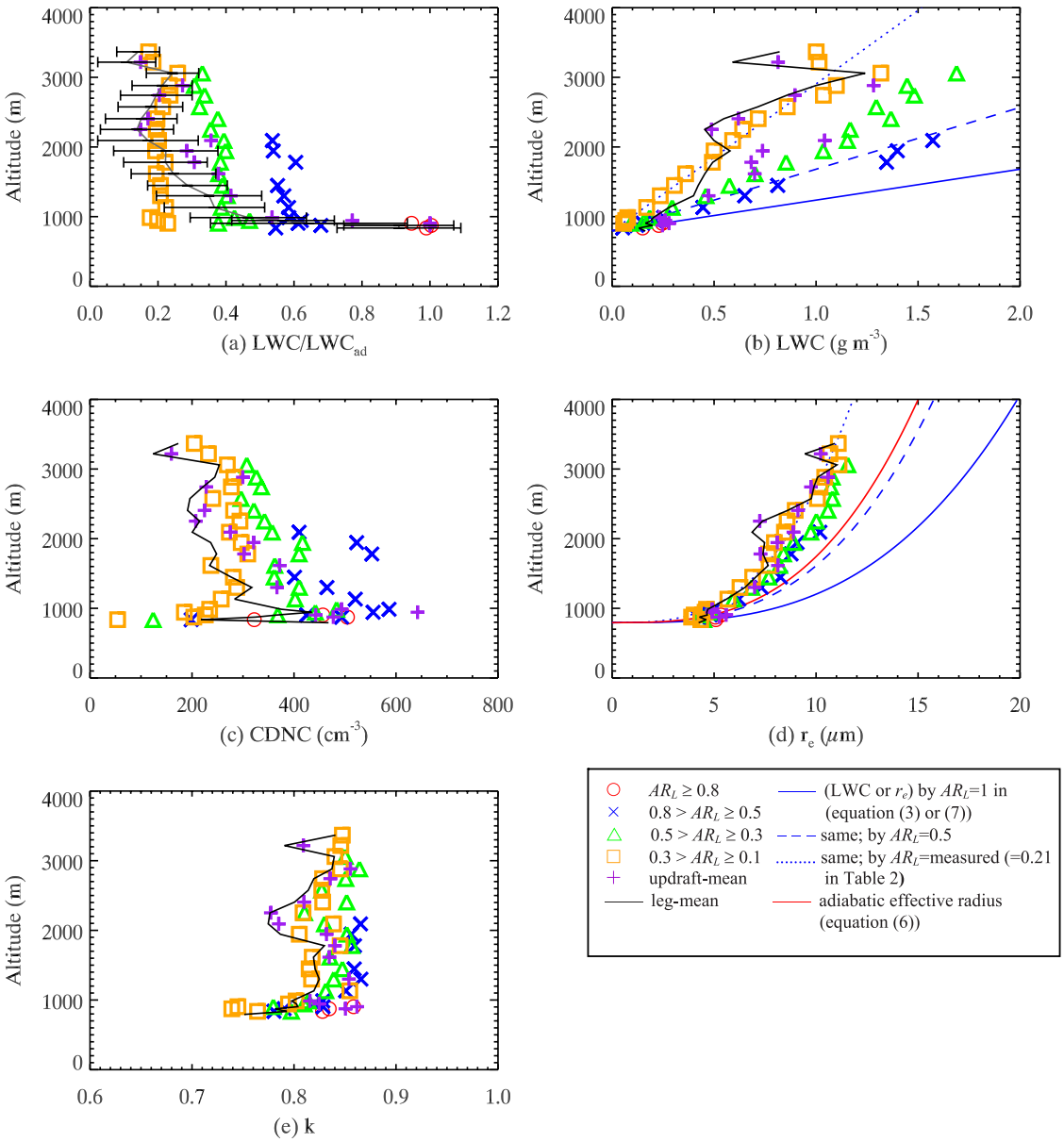


**Figure 6.** Properties of cloud RF18. Vertical profile of (a) adiabatic LWC ratio, (b) LWC, (c) cloud droplet number concentration, (d) effective radius, and (e) $k$ coefficient. $AR_L \geq 0.8$ is considered to be "quasi-adiabatic," $0.8 > AR_L \geq 0.5$ is "moderately diluted," and $0.5 > AR_L \geq 0.1$ is termed "strongly diluted."

adiabatic value. The $AR_L$ profile suggests entrainment mixing increases with height, in agreement with other cumulus studies (*Warner* [1970] and *Gerber* [2006, Table 1] from the Rain in Cumulus over the Ocean (RICO) experiment). Cumulus cloud is typically characterized by a central updraft core, the region that tends to be less influenced by entrainment. The updraft mean is calculated over the regions with updraft velocity >2 m s$^{-1}$. In Figures 6a and 6b, the updraft mean $AR_L$ is generally larger than the leg mean value throughout the cloud. Nevertheless, the updraft region is still "strongly diluted" for most of the cloud except near cloud base.

[26] The data indicated by the red circles in Figure 6 denote the average of those data points where the corresponding $AR_L$ exceeds 0.8. Clearly, the quasi-adiabatic region is present only near cloud base (Figure 6a, within 200 m). The cross symbols ($0.8 > AR_L \geq 0.5$) indicate that the moderately diluted region exists up to 1200 m above cloud base, which is about 0.5 cloud depth. From the middle of the cloud to cloud top, the cloud is strongly diluted ($AR_L$ = 0.1–0.3), and undiluted parcels were not encountered. The vertical extent of data indicated by these different symbols shows the extent to which the leg mean/updraft mean $AR_L$ decreases with height.

[27] Figure 6b presents vertical profiles of measured cloud LWC. The leg mean LWC for the most part increases with height. The dip near 2200–2700 m results because one of the two neighboring clouds that comprised RF18 had a lower cloud top around 2800 m. The updraft mean LWC is less affected by entrainment so it is generally larger than its

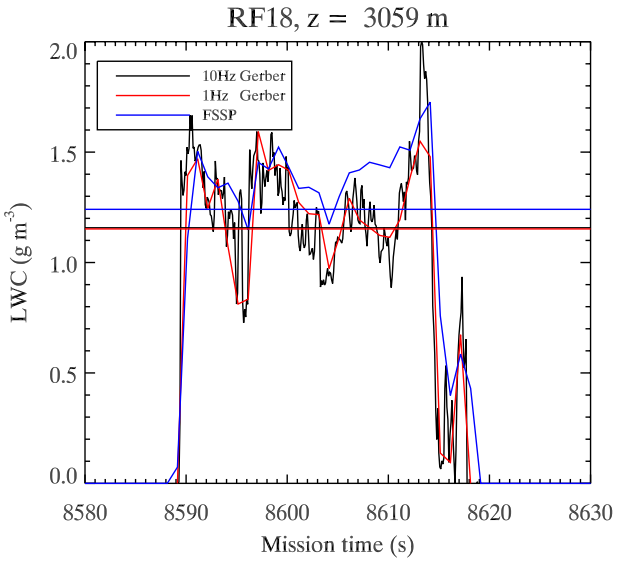


**Figure 7.** Time series of high-frequency PVM-100A (10 Hz), standard 1 Hz PVM-100A, and 1 Hz FSSP data for cloud RF18. The data are from a horizontal pass below cloud top. Horizontal lines are the leg mean values.

leg mean value. Both the leg mean and updraft mean LWC are much lower than the quasi-adiabatic LWC ($AR_L \geq 0.8$) except near cloud base. Above the middle of the cloud, the values of leg mean/updraft mean LWC are close to $0.3 > AR_L \geq 0.1$. These general features are in agreement with both the data in Figure 6a and the vertical distribution of CDNC in Figure 6c. In summary, the LWC and CDNC data suggest that the degree of subadiabaticity (dilution) increases with cloud height. Adiabatic parcels exist only up to several hundred meters above cloud base, which is in agreement with *Gerber* [2006].

[28] The significant entrainment mixing seen in the deep cloud RF18 affects cloud optical properties. The effect of entrainment mixing on cloud droplet effective radius is shown in Figure 6d. The various vertical profiles of effective radius (leg mean, updraft mean, and different $AR_L$'s) are more alike each other than the LWC and CDNC profiles because to first order, $r_e$ is dependent on the ratio of LWC and CDNC. Consistent with LWC observations, the leg mean and updraft mean effective radius values are close to the (quasi-) adiabatic value near cloud base; above cloud base, a considerable entrainment effect on reducing droplet effective radius is apparent. The adiabatic effective radius can be calculated from the adiabatic volume mean radius ($r_v$) through the relationship $r_e = k^{-1/3} r_v$ (see equation (2)). The value of $k$ can be obtained from Table 2, and is 0.84 for this case. From equation (4) and $LWC_{ad} = (4\pi\rho_w/3)\, CDNC_{ad}\, r_{v,ad}^3$, we can obtain the volume mean radius for an adiabatically vertically stratified cloud as $r_{v,ad}(h) = (b\, h/CDNC_{ad})^{1/3}$; therefore, from equation (2), the adiabatic effective radius is

$$r_{e,ad}(h) = \left(\frac{bh}{k\ CDNC_{ad}}\right)^{1/3}, \tag{6}$$

where $b = [C_w/(4\pi\rho_w/3)]$, and $\rho_w$ is water density. $CDNC_{ad}$ is the maximum CDNC in Table 2. The values of $k$ do not change significantly in the adiabatic and nonadiabatic regions (mostly within 10%, e.g., Figures 6e and 8e); therefore, in the above equation, we use the leg mean value of $k$. The subadiabatic effective radius can be calculated from equations (2)–(4) and $LWC = (4\pi\rho_w/3)\, CDNC\, r_v^3$ as,

$$r_e(h) = \left(\frac{AR_L bh}{k\ CDNC}\right)^{1/3}. \tag{7}$$

Near cloud base (within ~200 m), updraft mean LWC and effective radius are close to their adiabatic values; above this height to 0.2 × cloud depth, they can be approximated by equation (7) using $AR_L = 0.5$ (dashed line in Figure 6d); farther upward, close to the measured cloud top, $AR_L = 0.21$ (Table 2 and dotted line in Figure 6d).

#### 4.2.2. RF9_2 (Shallow Cumuli, Less Diluted Case)

[29] RF9_2 is a field of shallow cumuli, which exhibits the shallowest cloud depth among all those sampled (cloud depth ~400 m). One distinct feature as compared to the deep convective cloud RF18 is that this shallow cloud case exhibits less effect of entrainment mixing. The leg mean $AR_L$ of RF9_2 is about 0.85 to 0.5 from base to middle of the cloud, a value larger than that in the deep cloud (RF_18); it is about 0.3 near cloud top (Figure 8a). The vertical LWC profile (Figure 8b) shows that the leg mean and updraft mean LWC are close to the $AR_L = 0.5$ line (moderately diluted) in the middle of cloud. Near cloud top, the leg mean and updraft mean LWC are close to the region with $0.5 \geq AR_L \geq 0.3$ (strongly diluted). Similar to the deep cloud, the leg mean and updraft mean effective radius are also close to each other throughout the cloud depth for this shallow cumulus field (Figure 8d). The effective radius is close to its quasi-adiabatic value near cloud base. In the middle of the cloud, the updraft mean effective radius can be approximated by equation (7) with $AR_L = 0.5$; near cloud top $r_e$ is close to that predicted by equation (7) with observed cloud top $AR_L$.

### 4.3. Summary

[30] Applying the adiabatic ratio analysis on cloud LWC similar to Figure 6b to all clouds sampled (not shown except RF18 and RF9_2), we find that basically shallow clouds (RF2, RF9_1, and RF9_2, depth = 400–500 m) exhibit quasi-adiabatic regions extending from cloud base up to 0.5–1 × cloud depth ($H$). Deeper clouds with depths greater than 1700 m are dominated by strongly diluted regions throughout the cloud (RF12, RF15, RF18, RF19_1, and RF22, where RF12 is an exception with depth ~1000 m), with the quasi-adiabatic region existing only within several hundred meters above cloud base. Clouds with moderate cloud depths exhibited moderate dilution throughout cloud depth.

[31] From the above discussion, the degree of subadiabaticity is directly related to cloud depth. For this reason, the scatterplot of cloud top $AR_L$ (Table 2) is presented versus $H$ (Figure 9a). The regression result in Figure 9a is

$$AR_L(H) = -5.03 \times 10^{-5}\ H + 0.302, \tag{8}$$

where $H$ is in meters. Although the correlation is not strong ($R^2 = 0.36$), the data points in Figure 9a can be divided into three distinct groups, and equation (8) approximates the

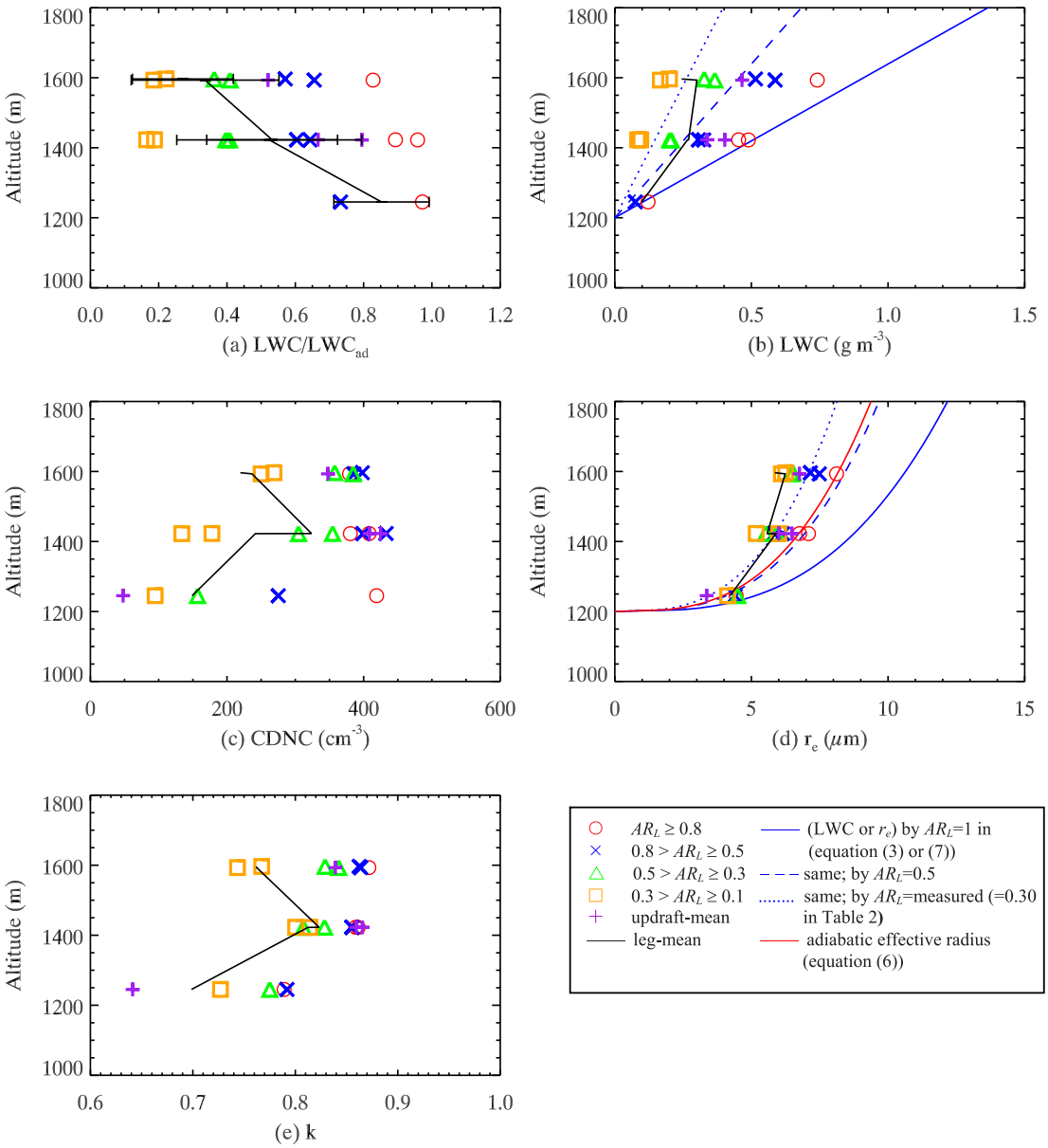


**Figure 8.** Same as Figure 6 but for cloud RF9_2.

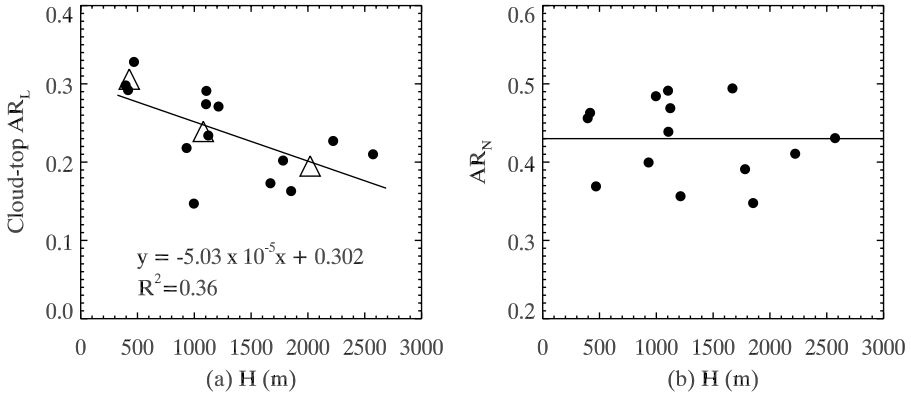


**Figure 9.** (a) Cloud top LWC and (b) cloud droplet number concentration adiabatic ratio as a function of cloud depth. Data points (circles) are from Table 2. Solid line in Figure 9a is the regression result of measurement data (circle). Triangles are the averaged results of three distinct groups of circles in Figure 9a. Solid line in Figure 9b is the constant line, $AR_N$ = 0.43.

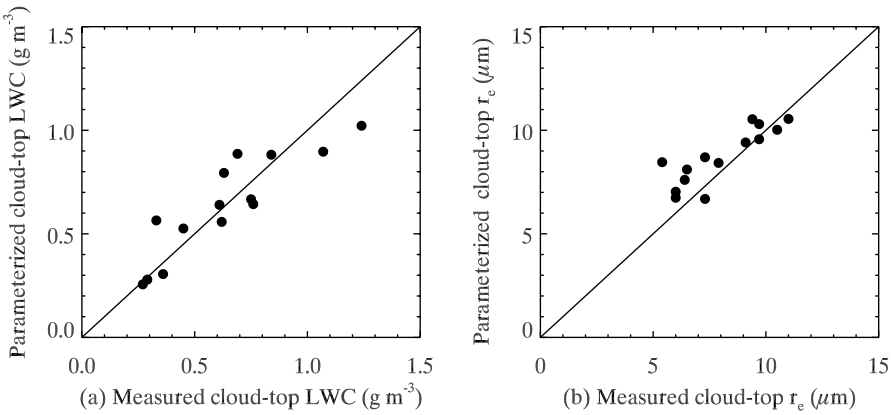


**Figure 10.** Comparison of measured (a) cloud top LWC and (b) cloud top effective radius with the parameterizations from equations (12) and (13), respectively, in the presence of entrainment mixing effects. Solid lines are the 1:1 lines.

means of these three groups (triangle symbols). From equations (7) and (8), one can calculate subadiabatic cloud top effective radius given that all the parameters are known. If applying equation (7), say, in a large-scale model, one also needs the relationship between subadiabatic CDNC and adiabatic CDNC. Similar to $AR_L$ in equation (3), the CDNC adiabatic ratio is defined as

$$AR_N = CDNC/CDNC_{ad},\ AR_N \le 1. \tag{9}$$

$AR_N$ is estimated for all sampled clouds from *CDNC* and maximum *CDNC* ($CDNC_{ad}$) in Table 2, and the values are plotted against $H$ in Figure 9b. In Figure 9b, $AR_N$ shows no correlation with $H$, and $AR_N$ can be represented by the average of all sampled clouds as

$$AR_N = 0.43 \pm 0.05. \tag{10}$$

From equations (7) and (9), we suggest the following parameterization of cloudy mean subadiabatic cloud top $r_e$, for cumulus clouds ($H$ = 400–2600 m) that are affected by entrainment mixing processes,

$$r_e(H) = \left(\frac{AR_L(H)}{AR_N}\,\frac{bH}{k\ CDNC_{ad}}\right)^{1/3}. \tag{11}$$

In this equation, $b$ and $H$ would be diagnosed from, say, a large or cloud-scale simulation, and $CDNC_{ad}$ is predicted by the activation scheme in the model [e.g., *Nenes and Seinfeld*, 2003]; $k$, $AR_L$, and $AR_N$ are empirical values/functions that are derived from the field measurements (e.g., $k$ = 0.78, $AR_N$ = 0.43, and $AR_L$ from equation (8) as shown in this study). By assuming $k$ = constant in the derivation, any effect of entrainment on $k$ is neglected.

[32] For an extremely inhomogeneous mixing scenario, $r_e = r_{e,ad}$, equation (11) implies $AR_L = AR_N$, meaning LWC and CDNC are diluted by the same degree from their adiabatic values. Figure 9 or Table 2 shows $AR_L < AR_N$ for all sampled clouds, and Figures 6 and 8 show $r_e < r_{e,ad}$, which suggest that sampled clouds exhibit some degrees of homogeneous mixing but rather not extremely inhomogeneous mixing from cloud-scale averaged properties.

[33] To evaluate these parameterizations, we first compare the parameterized cloud top LWC by equations (3), (4), and (8) at $h = H$ with measured cloud top LWC,

$$LWC(H) = AR_L(H)C_wH = \left(-5.03\times10^{-5}H^2 + 0.302H\right)C_w. \tag{12}$$

Results in Figure 10a show that parameterized cloud top LWC reasonably matches that measured, in which data points are generally close to the 1:1 line. The parameterized cloud top $r_e$ including the entrainment effect from equations (8), (10), and (11), is

$$r_e(H) = \left(\frac{(-11.7\times10^{-5}H^2 + 0.7H)b}{k\ CDNC_{ad}}\right)^{1/3}. \tag{13}$$

Figure 10b shows the parameterized cloud top $r_e$ and that measured reasonably adhere to the 1:1 line with deviation less than 15%.

[34] Beyond the dependence of entrainment on cloud depth, we also examine how entrainment depends on RH of the ambient environment. We calculate the ambient (clear sky) RH at each flight leg for all cloud cases. The results in Figure 11 show that there is no obvious correlation between ambient RH and $AR_L$ for all flight legs and cloud top leg of all clouds. Therefore, we did not find a dependence of entrainment on RH from our analysis.

### 4.4. Mixing Events

[35] Mixing events from two isolated clouds with numerous penetrations are selected and analyzed in this section. An evident cloud top entrainment event occurred in cloud RF18. Horizontal leg flight data of RF18 at two altitudes near cloud top are shown in Figure 12. In this plot, the red arrow highlights the region exhibiting entrainment mixing; to the right, the black arrows denote the undiluted (or less diluted) cloud region. LWC and CDNC are substantially lower in this mixing region than in the immediate cloudy undiluted region. This mixing region is also characterized by the presence of a downdraft. The temperature in the mixing region at the highest flight legs is lower than the ambient temperature (Figures 12a–12d); however, for

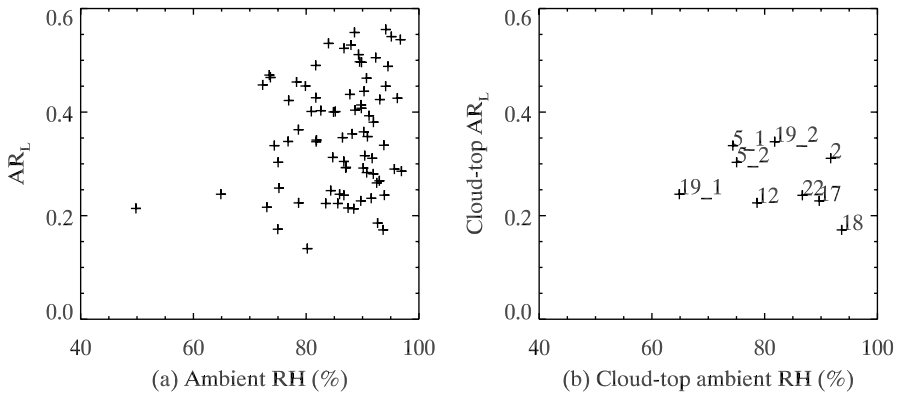


**Figure 11.** Relationship between entrainment ($AR_L$) and ambient RH for (a) all flight legs and (b) cloud top leg of all clouds.

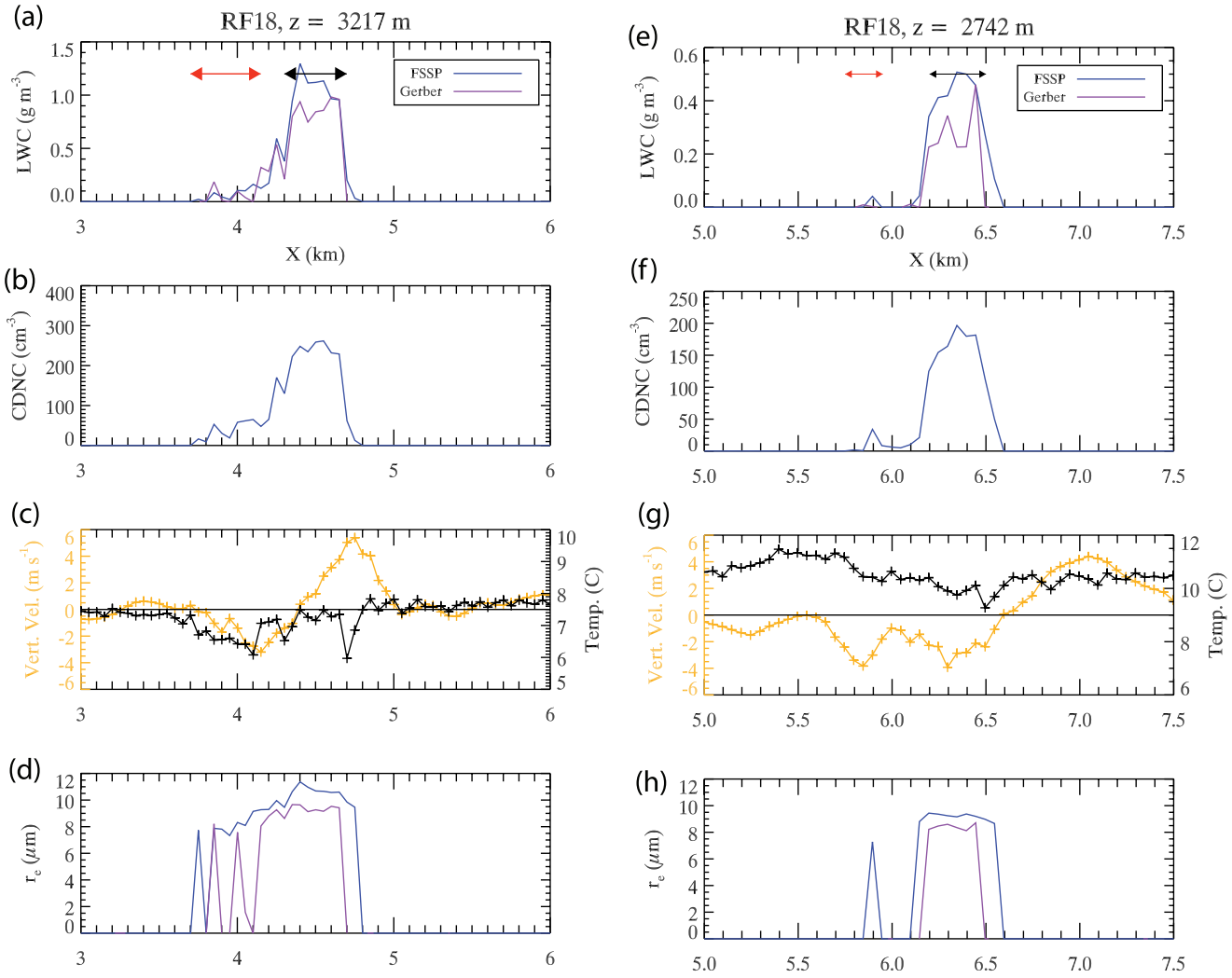


**Figure 12.** A mixing event near cloud top ($z$ = 3217 m; cloud top = 3367 m) for cloud RF 18. (a) Cloud LWC, (b) cloud droplet number concentration, (c) vertical velocity (left axis)/temperature (right axis), and (d) cloud effective radius. Horizontal axis is the horizontal distance. Red arrow denotes the region in which mixing occurred, and the black arrow denotes the undiluted region. (e–h) Another mixing event at height lower than Figures 12a–12d ($z$ = 2472 m; cloud top = 3367 m).

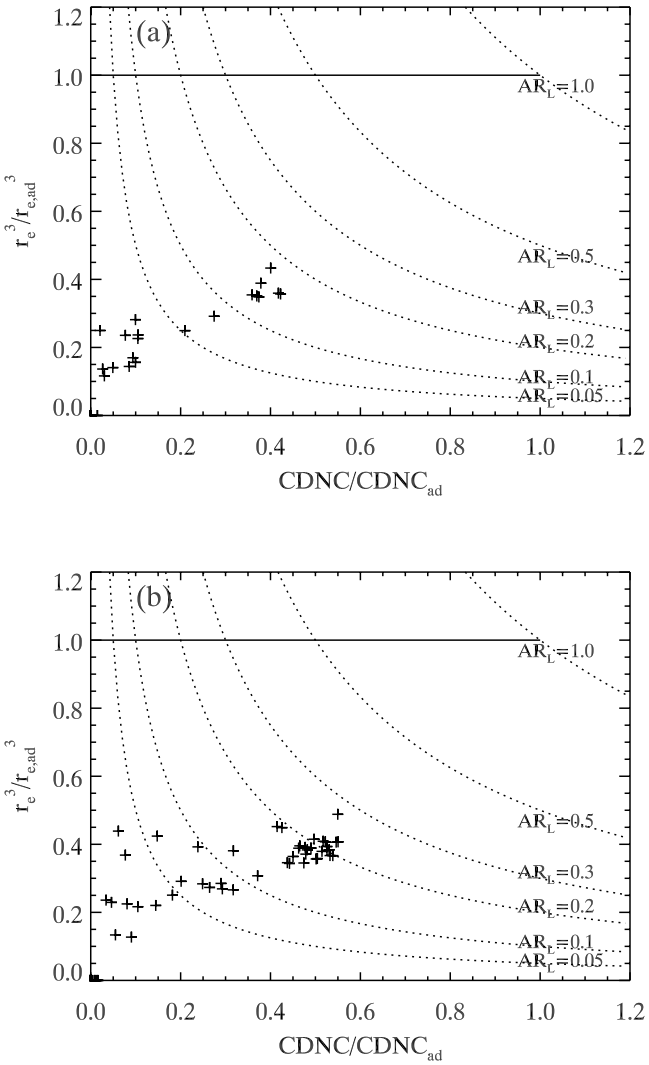


**Figure 13.** Microphysical mixing diagram of the effective radius and CDNC normalized by their adiabatic values. The horizontal solid line corresponds to extremely inhomogeneous mixing. The dotted contour lines represent different $AR_L$ values. Plus symbols denote data from the horizontal transect shown in (a) Figure 11a (RF18, z = 3217 m) and (b) Figure 11b (RF18, z = 2742 m).

the lower leg (Figures 12e–12h), the mixing region has a temperature similar to that in the unmixed cloudy region. These measurements suggest that evaporative cooling owing to entrainment mixing causes negative buoyancy and drives a downdraft [*Grabowski*, 1993]. For the leg closest to cloud top, the source of entrained air is possibly from above-cloud clear air. The effective radius is smaller in the mixing region.

[36] Figure 13 is a mixing diagram corresponding to the horizontal transect shown in Figure 12. As illustrated by *Burnet and Brenguier* [2007], this diagram can be used to examine the reductions in $r_e$ and CDNC owing to mixing process as a function of LWC dilution. Without mixing, $r_e$ and CDNC assume their adiabatic values, which is the (1, 1) point on the diagram. The contour lines on the diagram represent $AR_L$, which is the product of the coordinates derived from equations (6) and (7). The horizontal solid line denotes the extremely inhomogeneous mixing scenario, $r_e = r_{e,ad}$. The data points on Figure 13 show that the sampled cloud LWC for this leg are significantly diluted, with all data points having $AR_L < 0.3$. As the cloud LWC is more diluted toward smaller $AR_L$ values, both $r_e$ and CDNC deviate further from their adiabatic values. That the data points are all far below the horizontal solid line indicates that the mixing process is not extremely inhomogeneous. The results of $AR_L < AR_N$ of all sampled clouds shown in section 4.2.3 also support this argument.

[37] Another case of a single deep convective cloud (RF19_2) also exhibits smaller LWC, CDNC, effective radius, colder air, and downdraft in the mixing area of a horizontal pass near cloud top (Figure 14). In summary, three horizontal passes from two cloud cases show reduced CDNC and smaller droplet sizes in the mixing region, which are possible signatures of homogeneous mixing. We note that the analysis in this section is not a complete survey of mixing events from all sampled clouds.

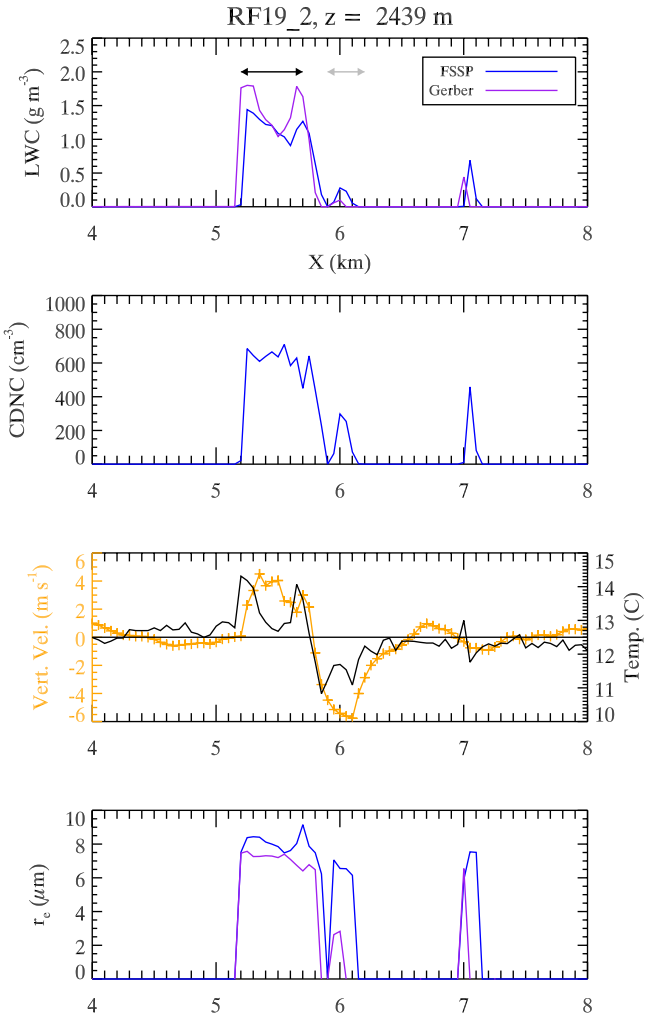


**Figure 14.** Mixing event during sampling of cloud RF19_2 near cloud top ($z$ = 2439 m).

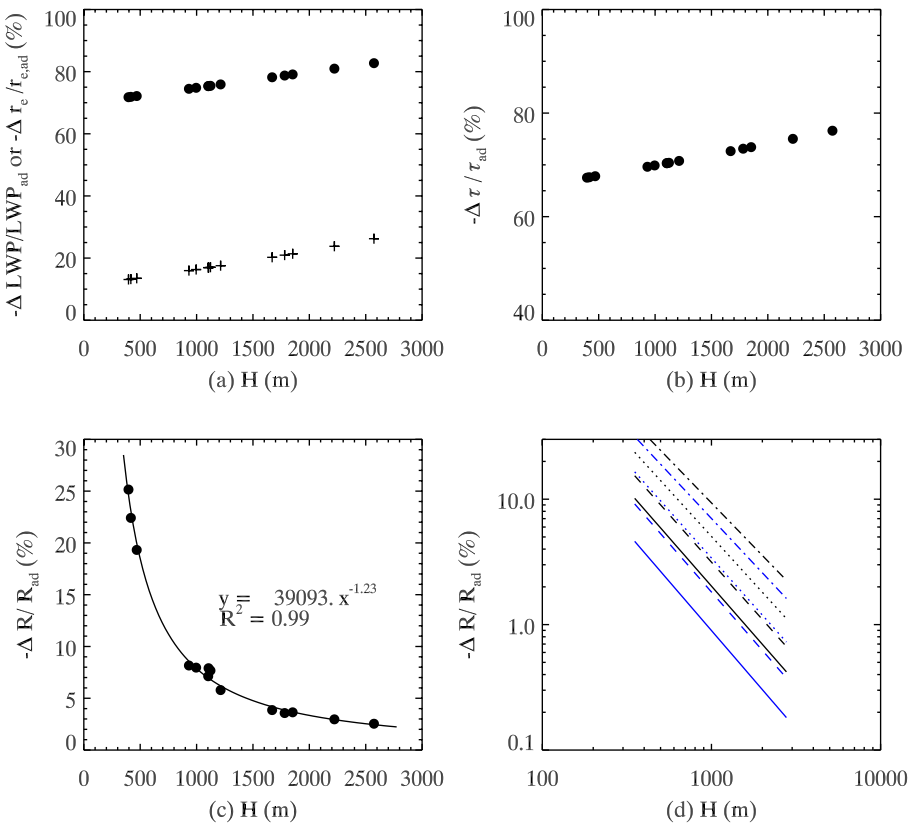


**Figure 15.** Overestimate of (a) cloud LWC (circle) and cloud top effective radius (plus), (b) cloud optical depth, and (c and d) cloud albedo for a vertically linear cloud LWC profile. $AR_L$ and $AR_N$ are calculated from equations (8) and (10). Solid line in Figure 15c is the regression result over the circles. Lines in Figure 15d are regression results of $-\Delta R/R_{ad}$ at different assumed values of $AR_L$ and $AR_N$.

### 4.5. Entrainment Mixing Impact on Cloud Optical Properties

[38] The impact of subadiabaticity owing to entrainment mixing on cloud optical properties has implications for aerosol indirect forcing. We estimate the effect of subadiabaticity on cloud properties, e.g., effective radius, LWP, cloud optical depth ($\tau$), and cloud albedo ($R$). The subadiabaticity effect on $x$, where $x$ comprises $\{r_e, LWP, \tau, R\}$, is calculated in terms of the change of $x$ with respect to its adiabatic value, that is, $-\Delta x/x_{ad}$. The deviation of the parameterized value ($x_{para}$) from its adiabatic value ($x_{ad}$) is represented by $\Delta x = x_{para} - x_{ad}$, and $x_{para}$ is parameterized on the basis of the observation. Because the measured/parameterized $x$ is always smaller than its adiabatic value, the effect of subadiabaticity on $x$ is represented by $-\Delta x/x_{ad}$.

### 4.6. Linear Vertical LWC Profile

[39] In this section, we assume a linearly vertically stratified cloud, which is frequently used in the literature, but is a simpler LWC profile than what is observed (see section 4.2). The subadiabaticity effect on effective radius is calculated from equations (6) and (11) at cloud top $h = H$,

$$-\frac{\Delta r_e}{r_{e,ad}} = 1 - \left(\frac{AR_L(H)}{AR_N}\right)^{1/3}. \tag{14}$$

Cloud liquid water path is calculated by $LWP = \int_0^H LWC(z)dz$, and with equation (3), we can get,

$$-\frac{\Delta LWP}{LWP_{ad}} = 1 - AR_L(H). \tag{15}$$

The adiabatic cloud optical depth is taken as $\tau_{ad} = 9\ LWP_{ad}/(5\ r_{e,ad}\ \rho_w)$ for an adiabatically, vertically stratified cloud [*Borg and Bennartz*, 2007]. The parameterized cloud optical depth is derived as

$$\tau_{para} = 2\pi \int_0^H CDNC r_s^2 dz = \frac{6}{5}\pi (AR_L(H)b)^{2/3}(k\ AR_N CDNC_{ad})^{1/3} H^{5/3}, \tag{16}$$

where $r_s$ is the surface mean radius. $-\Delta r_e/r_{e,ad}$, $-\Delta LWP/LWP_{ad}$, and $-\Delta\tau/\tau_{ad}$ are, as a result, functions of cloud depth. Figures 15a and 15b show that $-\Delta r_e/r_{e,ad}$, $-\Delta LWP/LWP_{ad}$, and $-\Delta\tau/\tau_{ad}$ are greater than zero, which means an overestimate of cloud LWP, $r_e$, and $\tau$ by using the adiabatic values; the overestimate increases with increasing $H$. The values of $-\Delta r_e/r_{e,ad}$, $-\Delta LWP/LWP_{ad}$, and $-\Delta\tau/\tau_{ad}$ range about 10–25%, 70–85%, and 65–80% over the sampled cloud depth, respectively. Also, LWP dominates over $r_e$ on the changes of $\tau$.

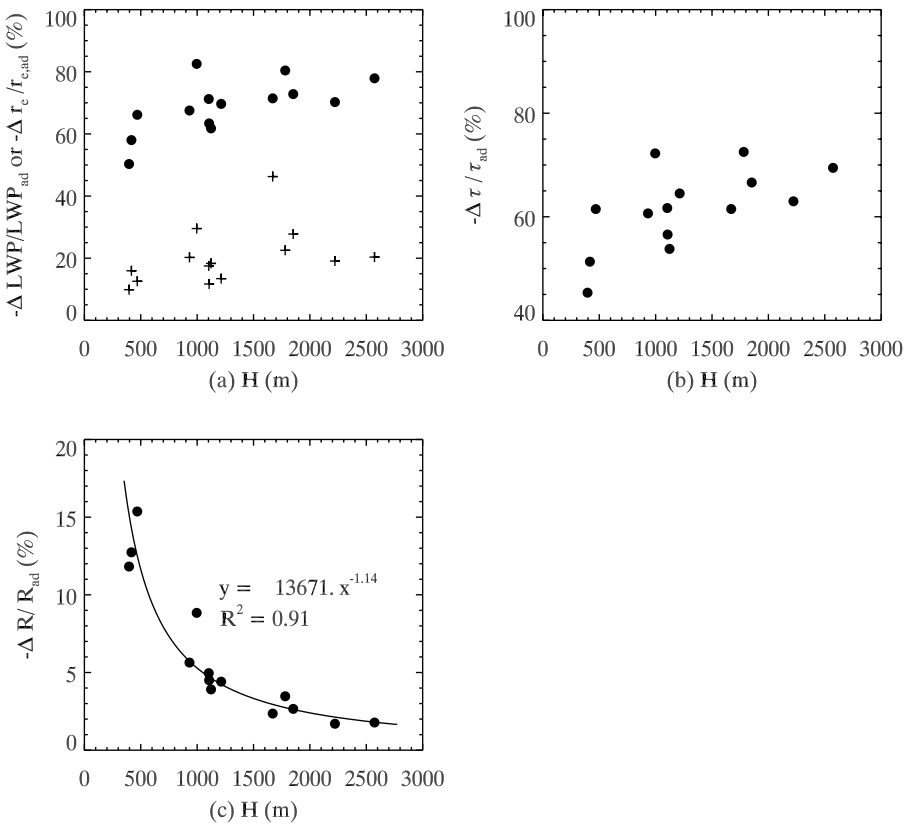


**Figure 16.** Similar to Figure 15 but for a quadratic form of vertical LWC profile.

[40] From the two-stream approximation for a nonabsorbing, horizontally homogeneous cloud with asymmetry factor of 0.85, cloud albedo is given by $R = \tau/(\tau + 7.7)$ [*Lacis and Hansen*, 1974]. The subadiabaticity effect on cloud albedo $-\Delta R/R_{ad}$ can therefore, be calculated by $\tau_{para}$ and $\tau_{ad}$. Similar to the concept of cloud susceptibility in the work by *Twomey* [1991], we can define the sensitivity of cloud albedo to the changes in cloud optical depth owing to entrainment. This is achieved by taking derivatives of $R$, and consequently

$$\Delta \ln R/\Delta \ln \tau = 7.7/(\tau + 7.7). \tag{17}$$

The sensitivity expression shows that $\Delta \ln R/\Delta \ln \tau$ is inversely proportional to $\tau$, and because $\tau \propto H$, equation (17) suggests that optically thin (shallow) clouds are more susceptible (vis-à-vis $R$) to entrainment effects than optically thick (deep) cloud. The calculation of $-\Delta R/R_{ad}$ for all the GoMACCS sampled clouds as a function of $H$ is shown in Figure 15c. The data points can be fitted with a power law relationship with a negative exponent, and therefore, $-\Delta R/R_{ad}$ decreases rapidly with $H$. Figure 15c also shows that the subadiabaticity results in an overestimate of cloud albedo of about 3–26% over the range of sampled $H$, and is about 20–26% for $H < 500$ m. Thus, entrainment mixing in shallow cumuli has a greater influence on cloud albedo than for a deeper cloud. As a result, the aerosol indirect effect is overestimated if entrainment mixing is not accounted for. The calculation is based on the plane-parallel assumption and therefore the 3-D radiative effect of cloud morphology is ignored.

[41] The sensitivities of $-\Delta R/R_{ad}$ to the value of $AR_L$ and $AR_N$ can be explored. Figure 15d shows the linear fitted lines of $-\Delta R/R_{ad}$ versus $H$ in log-log space for different assumed values of $AR_L$ and $AR_N$. In Figure 15d, values of $-\Delta R/R_{ad}$ increase with decreasing $AR_L$ and $AR_N$, which suggest that the larger the entrainment effects on either LWC or CDNC, the larger the relative change of cloud albedo owing to entrainment to its adiabatic value. When $AR_L \leq 0.6$ and $AR_N \leq 0.4$ for $H \leq 500$ m, $-\Delta R/R_{ad}$ exceeds 10%.

### 4.7. Quadratic Vertical LWC Profile

[42] The $AR_L$ analysis in section 4.2 shows the vertical LWC profile is closer to a quadratic form, especially the deep cloud that exhibits stronger entrainment effect toward the cloud top. We, therefore, demonstrate the subadiabaticity effect on the cloud optical properties based on a quadratic LWC profile. The vertical cloud LWC profile is assumed to be of the functional form, $LWC_{para}(z) = az^2 + bz$, where $a$ and $b$ are coefficients obtained from fitting of the observed data. The cloud LWP is thus, from its definition, as $LWP_{para} = \frac{a}{3}H^3 + \frac{b}{2}H^2$. Cloud top effective radius can be obtained from equation (2),

$$r_{e,para} = k^{-1/3}\left(\frac{LWC(H)}{\frac{4}{3}\pi\rho_w AR_N CDNC_{ad}}\right)^{1/3}. \tag{18}$$

Finally, we can get the parameterized cloud optical depth similar to equation (16),

$$\tau_{para} = 2\pi (AR_N CDNC_{ad} k)^{1/3} \left(\frac{4}{3}\pi\rho_w\right)^{-2/3} \int_0^H LWC(z)^{2/3} dz. \quad (19)$$

Using the above derived parameters, the subadiabaticity effects can be calculated. Figure 16 shows similar results to the linear LWC profile in Figure 15: $-\Delta r_e/r_{e,ad}$, $-\Delta LWP/LWP_{ad}$, and $-\Delta\tau/\tau_{ad}$ increase with increasing $H$; $-\Delta R/R_{ad}$ decreases exponentially with $H$. The values of $-\Delta r_e/r_{e,ad}$, $-\Delta LWP/LWP_{ad}$, $-\Delta\tau/\tau_{ad}$, and $-\Delta R/R_{ad}$ range about 5–35%, 50–85%, 45–75%, and 2–16% over the sampled cloud depth, respectively. The value of $-\Delta R/R_{ad}$ of the quadratic model shows a smaller value (11–15%) for $H <$ 500 m than that of the linear model. In summary, the vertically quadratic LWC profile yields results similar to those based on the linear LWC profile.

## 5. Conclusion

[43] We report aerosol-cloud relationships from 14 scattered and isolated warm continental cumuli sampled over the Houston region during 2006 August–September GoMACCS campaign. The sampled clouds occurred under a wide range of anthropogenic influence with total subcloud aerosol number concentrations ranging between 1400 and 11,500 $cm^{-3}$. The cloud-scale averaged results clearly exhibit aerosol effects on cloud microphysics; cloud droplet number concentration is found to be proportional to the subcloud accumulation mode aerosol number concentration according to the power law relationship, $CDNC = 15.3\ N_{acc}^{0.43}$ ($N_{acc}$ = 400–1650 $cm^{-3}$); CDNC is best represented by equation (1) when considering both $N_{acc}$ and cloud base updraft. The cloud top effective radius is inversely proportional to the subcloud aerosol number concentration, after accounting for the dependence of cloud top effective radius on cloud depth, $r_e/H^3 = 5.6\ N_{acc}^{-0.30}$. There are no discernable aerosol impacts on cloud spectral relative dispersion; the clouds exhibit nearly constant values of $d = 0.30 \pm 0.04$ and $k = 0.78 \pm 0.05$, respectively. Comparisons of two isolated cloud cases show that the polluted cloud has higher CDNC, smaller $r_e$ and drizzle drops, and weaker precipitation than the clean cloud.

[44] Clouds are found to have been strongly influenced by entrainment mixing processes, resulting in subadiabaticity of cloud LWC, with the entrainment effect on cloud LWC increasing with cloud depth. The vertical extent of the quasi-adiabatic region basically depends on cloud depth: for deep clouds (>1700 m thickness), the quasi-adiabatic region extends only a few hundred meters above cloud base; for shallow clouds (= 400–500 m thickness), it can approach cloud top. Entrainment mixing causes reductions in cloud droplet number concentration and cloud top effective radius relative to the corresponding adiabatic values. Three horizontal passes close to two cloud tops show the presence of mixing events. Evaporative cooling resulting from mixing of the entrained above-cloud ambient air with the cloudy air drives the cloud edge downdraft. From the overall averaged cloud properties of the warm continental cumulus clouds sampled (cloud depth $H$ = 400–2600 m), the following parameterization for cloudy mean cloud top effective radius can be derived,

$$r_e(H) = \left(\frac{AR_L(H)}{AR_N}\frac{bH}{k\ CDNC_{ad}}\right)^{1/3},$$

where $CDNC_{ad}$ is the adiabatic cloud droplet number concentration, as predicted, for example, by a large or cloud-scale model. $AR_L$ and $AR_N$ are the adiabatic ratio of LWC and CDNC, respectively, and $k = r_v^3/r_e^3$. $AR_L$, $AR_N$, and $k$ can be derived from field observations (e.g., $k = 0.78$, $AR_N = 0.43$, and $AR_L = AR_L(H)$ from equation (8) as shown in this study). This parameterized cloud top effective radius generally agrees with the GoMACCS data.

[45] For the clouds sampled, cloud LWP, effective radius, cloud optical depth, and cloud albedo, based on the plane-parallel assumption, are predicted to be decreased by 50–85%, 5–35%, 45–85%, and 2–26%, respectively, as a result of subadiabaticity. The vertically linear LWC profile and the vertically quadratic LWC profile generally show similar results. The entrainment effect on cloud albedo is largest for shallow cumuli, which is about $-\Delta R/R_{ad}$ = 20–26% (11–15%) for cloud depth smaller than 500 m of a vertically linear (quadratic) LWC profile. The relative change of cloud albedo owing to subadiabaticity is found to increase with increasing entrainment. The entrainment process has a much larger effect on cloud LWP (and thus cloud optical depth) than cloud top effective radius and cloud albedo, which suggests that an accurate value of LWC or LWP is of first-order importance. The current sensitivity analysis is based on plane-parallel clouds, 3-D cloud morphology radiative effects (scattering of photons between clouds) and cloud fraction changes could be influential. For example, from 3-D radiative transfer calculations, *Chosson et al.* [2007] conclude that the plane-parallel approximation may substantially overestimate the albedo of a spatially heterogeneous cloud under two extreme mixing scenarios. *Zuidema et al.* [2008] show that cloud fraction changes as a result of droplet evaporative cooling induced by entrainment mixing could also affect the aerosol indirect effect. Cloud radiative properties are sensitive to LWP, and drizzle initiation is sensitive to cloud droplet radius; therefore, including entrainment effects on the subgrid parameterization for GCM cloud microphysics and radiative transfer calculation may be important in improving the accuracy of simulating aerosol indirect effects in large-scale models.

[46] **Acknowledgment.** This work was supported by National Oceanic and Atmospheric Administration grant NA06OAR4310082.

## References

Baker, M. B., and J. Latham (1979), Evolution of droplet spectra and the rate of production of embryonic raindrops in small cumulus clouds, *J. Atmos. Sci.*, *36*, 1612–1615, doi:10.1175/1520-0469(1979)036<1612:TEODSA>2.0.CO;2.

Baker, M. B., R. G. Corbin, and J. Latham (1980), The influence of entrainment on the evolution of cloud droplet spectra. I. A model of inhomogeneous mixing, *Q. J. R. Meteorol. Soc.*, *106*, 581–598, doi:10.1002/qj.49710644914.

Baumgardner, D., W. Strapp, and J. E. Dye (1985), Evaluation of the forward scattering spectrometer probe. Part II: Corrections for coincidence and dead-time losses, *J. Atmos. Oceanic Technol.*, *2*, 626–632, doi:10.1175/1520-0426(1985)002<0626:EOTFSS>2.0.CO;2.

Blyth, A. M., and J. Latham (1985), An airborne study of vertical structure and microphysical variability within a small cumulus, *Q. J. R. Meteorol. Soc.*, *111*, 773–792, doi:10.1256/smsqj.46906.

Boers, R., H. Russchenberg, J. Erkelens, V. Venema, A. van Lammeren, A. Apituley, and S. Jongen (2000), Ground-based remote sensing of stratocumulus properties during CLARA, 1996, *J. Appl. Meteorol.*, *39*, 169–181, doi:10.1175/1520-0450(2000)039<0169:GBRSOS>2.0.CO;2.

Boers, R., J. R. Acarreta, and J. L. Gras (2006), Satellite monitoring of the first indirect aerosol effect: Retrieval of the droplet concentration of water clouds, *J. Geophys. Res.*, *111*, D22208, doi:10.1029/2005JD006838.

Bolton, D. (1980), The computation of equivalent potential temperature, *Mon. Weather Rev.*, *108*, 1046–1053, doi:10.1175/1520-0493(1980)108<1046:TCOEPT>2.0.CO;2.

Borg, L. A., and R. Bennartz (2007), Vertical structure of stratiform marine boundary layer clouds and its impact on cloud albedo, *Geophys. Res. Lett.*, *34*, L05807, doi:10.1029/2006GL028713.

Brenguier, J.-L. (1991), Parameterization of the condensation process - A theoretical approach, *J. Atmos. Sci.*, *48*, 264–282, doi:10.1175/1520-0469(1991)048<0264:POTCPA>2.0.CO;2.

Brenguier, J.-L., H. Pawlowska, L. Schuller, R. Preusker, J. Fischer, and Y. Fouquart (2000), Radiative properties of boundary layer clouds: Droplet effective radius versus number concentration, *J. Atmos. Sci.*, *57*, 803–821, doi:10.1175/1520-0469(2000)057<0803:RPOBLC>2.0.CO;2.

Burnet, F., and J.-L. Brenguier (2007), Observational study of the entrainment-mixing process in warm convective clouds, *J. Atmos. Sci.*, *64*, 1995–2011, doi:10.1175/JAS3928.1.

Chosson, F., J.-L. Brenguier, and L. Schueller (2007), Entrainment-mixing and radiative transfer simulation in boundary layer clouds, *J. Atmos. Sci.*, *64*, 2670–2682, doi:10.1175/JAS3975.1.

Chuang, P. Y., J. D. Small, E. W. Saw, R. A. Shaw, C. M. Sipperley, G. A. Payne, W. D. Bachalo, H. Siebert, F. Burnet, and J.-L. Brenguier (2008), Airborne Phase Doppler Interferometry for cloud microphysical measurements, *Aerosol Sci. Technol.*, in press.

Feingold, G. (2003), Modeling of the first indirect effects: Analysis of measurement requirements, *Geophys. Res. Lett.*, *30*(19), 1997, doi:10.1029/2003GL017967.

Feingold, G., W. L. Eberhard, D. E. Veron, and M. Previdi (2003), First measurements of the Twomey indirect effect using ground-based remote sensors, *Geophys. Res. Lett.*, *30*(6), 1287, doi:10.1029/2002GL016633.

Gerber, H. (2006), Entrainment, mixing, and microphysics in RICO cumulus, paper presented at 12th Conference on Cloud Physics, Am. Meteorol. Soc., Madison, Wis.

Gerber, H., B. G. Arends, and A. S. Ackerman (1994), New microphysics sensor for aircraft use, *Atmos. Res.*, *31*, 235–252, doi:10.1016/0169-8095(94)90001-9.

Grabowski, W. W. (1993), Cumulus entrainment, fine-scale mixing, and buoyancy reversal, *Q. J. R. Meteorol. Soc.*, *119*, 935–956, doi:10.1002/qj.49711951305.

Gultepe, I., G. A. Isaac, W. R. Leaitch, and C. M. Banic (1996), Parameterizations of marine stratus microphysics based on in situ observations: Implications for GCMs, *J. Clim.*, *9*, 345–357, doi:10.1175/1520-0442(1996)009<0345:POMSMB>2.0.CO;2.

Jiang, H., G. Feingold, H. H. Jonsson, M.-L. Lu, P. Y. Chuang, R. C. Flagan, and J. H. Seinfeld (2008), Statistical comparison of properties of simulated and observed cumulus clouds in the vicinity of Houston during the Gulf of Mexico Atmospheric Composition and Climate Study (GoMACCS), *J. Geophys. Res.*, *113*, D13205, doi:10.1029/2007JD009304.

Jirak, I. L., and W. R. Cotton (2006), Effect of air pollution on precipitation along the front range of the Rocky Mountains, *J. Appl. Meteorol. Climatol.*, *45*, 236–245, doi:10.1175/JAM2328.1.

Kaufman, Y. J., and I. Koren (2006), Smoke and pollution aerosol effect on cloud cover, *Science*, *313*, 655–658, doi:10.1126/science.1126232.

Kim, B. G., S. E. Schwartz, M. A. Miller, and Q. L. Min (2003), Effective radius of cloud droplets by ground-based remote sensing: Relationship to aerosol, *J. Geophys. Res.*, *108*(D23), 4740, doi:10.1029/2003JD003721.

Lacis, A. A., and J. E. Hansen (1974), A parameterization for the absorption of solar radiation in the Earth's atmosphere, *J. Atmos. Sci.*, *31*, 118–133, doi:10.1175/1520-0469(1974)031<0118:APFTAO>2.0.CO;2.

Leaitch, W. R., J. W. Strapp, G. A. Isaac, and J. G. Hudson (1986), Cloud droplet nucleation and cloud scavenging of aerosol sulphate in polluted atmospheres, *Tellus, Ser. B*, *38*, 328–344.

Liu, Y., and P. H. Daum (2002), Anthropogenic aerosols: Indirect warming effect from dispersion forcing, *Nature*, *419*, 580–581, doi:10.1038/419580a.

Liu, Y., and P. H. Daum (2004), Parameterization of the autoconversion process. Part I: Analytical formulation of the Kessler-type parameterizations, *J. Atmos. Sci.*, *61*, 1539–1548, doi:10.1175/1520-0469(2004)061<1539:POTAPI>2.0.CO;2.

Lu, M.-L., and J. H. Seinfeld (2006), Effect of aerosol number concentration on cloud droplet dispersion: A large-eddy simulation study and implications for aerosol indirect forcing, *J. Geophys. Res.*, *111*, D02207, doi:10.1029/2005JD006419.

Lu, M.-L., W. C. Conant, H. H. Jonsson, V. Varutbangkul, R. C. Flagan, and J. H. Seinfeld (2007), The Marine Stratus/Stratocumulus Experiment (MASE): Aerosol-cloud relationships in marine stratocumulus, *J. Geophys. Res.*, *112*, D10209, doi:10.1029/2006JD007985.

Martin, G. M., D. W. Johnson, and A. Spice (1994), The measurement and parameterization of effective radius of droplets in warm stratocumulus clouds, *J. Atmos. Sci.*, *51*, 1823–1842, doi:10.1175/1520-0469(1994)051<1823:TMAPOE>2.0.CO;2.

Mason, B. J., and P. R. Jonas (1974), Evolution of droplet spectra and large droplets by condensation in cumulus clouds, *Q. J. R. Meteorol. Soc.*, *100*, 23–38, doi:10.1002/qj.49710042304.

McFarquhar, G. M., and A. J. Heymsfield (2001), Parameterizations of INDOEX microphysical measurements and calculations of cloud susceptibility: Applications for climate studies, *J. Geophys. Res.*, *106*, 28,675–28,698, doi:10.1029/2000JD900777.

Miles, N. L., J. Verlinde, and E. E. Clothiaux (2000), Cloud droplet size distributions in low-level stratiform clouds, *J. Atmos. Sci.*, *57*, 295–311, doi:10.1175/1520-0469(2000)057<0295:CDSDIL>2.0.CO;2.

Nenes, A., and J. H. Seinfeld (2003), Parameterization of cloud droplet formation in global climate models, *J. Geophys. Res.*, *108*(D14), 4415, doi:10.1029/2002JD002911.

Paluch, I. R. (1979), Entrainment mechanism in Colorado cumuli, *J. Atmos. Sci.*, *36*, 2467–2478, doi:10.1175/1520-0469(1979)036<2467:TEMICC>2.0.CO;2.

Pawlowska, H., W. W. Grabowski, and J.-L. Brenguier (2006), Observations of the width of cloud droplet spectra in stratocumulus, *Geophys. Res. Lett.*, *33*, L19810, doi:10.1029/2006GL026841.

Penner, J. E., X. Dong, and Y. Chen (2004), Observational evidence of a change in radiative forcing due to the indirect aerosol effect, *Nature*, *427*, 231–234, doi:10.1038/nature02234.

Pilewskie, P., J. Pommier, R. Bergstrom, W. Gore, S. Howard, M. Rabbette, B. Schmid, P. V. Hobbs, and S. C. Tsay (2003), Solar spectral radiative forcing during the Southern African Regional Science Initiative, *J. Geophys. Res.*, *108*(D13), 8486, doi:10.1029/2002JD002411.

Raga, G. B., and P. R. Jonas (1993), On the link between cloud-top radiative properties and sub-cloud aerosol concentrations, *Q. J. R. Meteorol. Soc.*, *119*, 1419–1425, doi:10.1002/qj.49711951410.

Raga, G. B., J. B. Jensen, and M. B. Baker (1990), Characteristics of cumulus band clouds off the coast of Hawaii, *J. Atmos. Sci.*, *47*, 338–355, doi:10.1175/1520-0469(1990)047<0338:COCBCO>2.0.CO;2.

Roberts, G. C., and A. Nenes (2005), A continuous-flow streamwise thermal-gradient CCN chamber for atmospheric measurements, *Aerosol Sci. Technol.*, *39*, 206–221, doi:10.1080/027868290913988.

Rosenfeld, D., and I. M. Lensky (1998), Satellite-based insights into precipitation formation processes in continental and maritime convective clouds, *Bull. Am. Meteorol. Soc.*, *79*, 2457–2476, doi:10.1175/1520-0477(1998)079<2457:SBIIPF>2.0.CO;2.

Seinfeld, J. H., and S. N. Pandis (2006), *Atmospheric Chemistry and Physics: From Air Pollution to Climate Change*, 2nd ed., 1232 pp., John Wiley, Hoboken, N. J.

Sorooshian, A., F. J. Brechtel, Y. L. Ma, R. J. Weber, R. C. Corless, R. C. Flagan, and J. H. Seinfeld (2006), Modeling and characterization of a particle-into-liquid sampler (PILS), *Aerosol Sci. Technol.*, *40*, 396–409.

Sorooshian, A., N. L. Ng, A. W. H. Chan, G. Feingold, R. C. Flagan, and J. H. Seinfeld (2007), Particulate organic acids and overall water-soluble aerosol composition measurements from the 2006 Gulf of Mexico Atmospheric Composition and Climate Study (GoMACCS), *J. Geophys. Res.*, *112*, D13201, doi:10.1029/2007JD008537.

Twomey, S. (1991), Aerosols, clouds and radiation, *Atmos. Environ.*, *25*, 2435–2442.

Warner, J. (1955), The water content of cumuliform clouds, *Tellus*, *7*, 449–457.

Warner, J. (1968), A reduction in rainfall associated with smoke from sugar-cane fires—An inadvertent weather modification?, *J. Appl. Meteorol.*, *7*, 247–251, doi:10.1175/1520-0450(1968)007<0247:ARIRAW>2.0.CO;2.

Warner, J. (1970), On steady-state one-dimensional models of cumulus convection, *J. Atmos. Sci.*, *27*, 1035, doi:10.1175/1520-0469(1970)027<1035:OSSODM>2.0.CO;2.

Warner, J. (1971), Smoke from sugar-cane fires and rainfall, paper presented at International Conference on Weather Modification, American Meteorological Society, Canberra, A. C. T.

Warner, J. (1973), Microstructure of cumulus cloud. Part 4: Effect on droplet spectrum of mixing between cloud and environment, *J. Atmos. Sci.*, *30*, 256–261, doi:10.1175/1520-0469(1973)030<0256:TMOCCP>2.0.CO;2.

Zuidema, P., H. Xue, and G. Feingold (2008), Shortwave radiative impacts from aerosol effects on marine shallow cumuli, *J. Atmos. Sci.*, *65*, 1979–1990.

P. Y. Chuang, Department of Earth and Planetary Sciences, University of California, Santa Cruz, CA 95064, USA.

G. Feingold, Chemical Sciences Division, Earth System Research Laboratory, NOAA, Boulder, CO 80305, USA.

R. C. Flagan, M.-L. Lu, and J. H. Seinfeld, Department of Environmental Science and Engineering, California Institute of Technology, 1200 East California Boulevard, Mail Code 210-41, Pasadena, CA 91125, USA. (seinfeld@caltech.edu)

H. Gates, Department of Chemical Engineering, California Institute of Technology, Pasadena, CA 91125, USA.

H. H. Jonsson, Department of Meteorology, Naval Postgraduate School, Monterey, CA 93943, USA.